

1 **Dynamically Downscaled Future Projections of the Northwest Atlantic Ocean**  
2 **Across Low to High Emissions Scenarios**

3  
4 Dongmin Kim<sup>1,2</sup>, Andrew C. Ross<sup>3</sup>, Sang-Ik Shin<sup>4,5</sup>, Fabian A. Gomez<sup>6,2</sup>, Jasmin G. John<sup>2</sup>,  
5 Denis L. Volkov<sup>1,2</sup>, Sang-Ki Lee<sup>2</sup>, Michael A. Alexander<sup>7</sup> and Charles A. Stock<sup>3</sup>

6  
7 <sup>1</sup>Cooperative Institute for Marine and Atmospheric Studies, University of Miami, Miami, FL,  
8 USA

9 <sup>2</sup>NOAA/OAR/Atlantic Oceanographic & Meteorological Laboratory, Miami, FL, USA

10 <sup>3</sup>NOAA/OAR/Geophysical Fluid Dynamics Laboratory, Princeton, NJ, USA,

11 <sup>4</sup>Cooperative Institute for Research in Environmental Sciences, University of Colorado Boulder,  
12 Boulder, CO, USA,

13 <sup>5</sup>NOAA/OAR/Physical Sciences Laboratory, Boulder, CO, USA,

14 <sup>6</sup>Northern Gulf Institute, Mississippi State University, Starkville, MS, USA

15 <sup>7</sup>Department of Atmospheric and Oceanic Sciences, University of Colorado Boulder, Boulder,  
16 CO, USA

17  
18  
19  
20 **Corresponding author:** Dr. Dongmin Kim ([dongmin.kim@noaa.gov](mailto:dongmin.kim@noaa.gov)), Cooperative Institute for  
21 Marine and Atmospheric Studies, University of Miami, 4600 Rickenbacker Causeway, Miami, FL  
22 33149, USA.

24 **Abstract**

25 We used a high-resolution (1/12°) Modular Ocean Model version 6 implementation for the  
26 the Northwest Atlantic Ocean (MOM6-NWA12) to dynamically downscale Geophysical Fluid  
27 Dynamics Laboratory Earth System Model version 4.1 (GFDL-ESM4.1) projections for the 21st  
28 century. Simulations were conducted under four different Coupled Model Intercomparison  
29 Project Phase 6 emission scenarios. MOM6-NWA12 accurately simulates the spatial patterns of  
30 sea surface temperature, salinity, and dynamic sea surface height (SSH) during the historical  
31 period. In particular, the Gulf Stream's strength, position, recirculation, and separation from the  
32 U.S. East Coast are significantly improved in MOM6-NWA12 compared to the coarse-resolution  
33 GFDL-ESM4.1. Projected end-of-century warming varied strongly between scenarios, from ~  
34 4 °C under prior "worst case" emissions scenarios (SSP-585), 2~3 °C under intermediate  
35 scenarios (SSP-245, SSP-370) more consistent with current trajectories, to ~ 1 °C under  
36 aggressive mitigation (SSP-126). Consistent with a significant weakening of the Atlantic  
37 Meridional Overturning Circulation projected by GFDL-ESM4.1, MOM6-NWA12 shows a  
38 substantial volume transport reduction in the Western Boundary Current (WBC) system (i.e.,  
39 Yucatan Current, Florida Current, Antilles Current, and the Deep Western Boundary Current)  
40 toward the late 21st century (between 23 and 38 %, varying by scenario). This projected  
41 weakening of the WBC system and the associated reduction in the coastal upwelling of cold,  
42 fresh subsurface waters lead to a significant increase in ocean temperature, salinity, and dynamic  
43 SSH along the U.S. southeast and northeast Coasts, particularly in the South Atlantic Bight.

44

45 **1. Introduction**

46 The Northwest Atlantic Ocean (NWA), including the United States (US) East and Gulf  
47 Coasts, and the Caribbean Sea, is characterized by large spatial heterogeneity in ocean conditions  
48 and complex interactions between ocean circulation and biogeochemistry (e.g., Wang et al.,  
49 2013; Muller-Karger et al., 2015; Wanninkhof et al., 2015; Gomez et al., 2020; 2022; Friedrichs  
50 et al., 2019; Zhang et al., 2023). A myriad of living marine resources inhabit this region,  
51 including the South Florida coral reefs, lobsters and shellfish, demersal fish species like  
52 groupers, snappers, cod and haddock, and migratory pelagic fish species like bluefin tuna and  
53 king mackerel, all of whose distribution and abundance are influenced by changes in ocean  
54 temperature and circulation (e.g., Weinberg 2005; Bell et al., 2015; Karnauskas et al., 2013,  
55 2015; Tanaka et al., 2020). Previous studies have shown that portions of the ocean ecosystem are  
56 modulated by large scale climate variability, such as El Niño Southern Oscillation and Atlantic  
57 Multidecadal Oscillation, through associated changes in ocean circulation and river runoff (e.g.,  
58 Alexander and Scott, 2008; Gomez et al., 2019, 2024). Moreover, the region is undergoing  
59 sustained warming, particularly along the US South and East Coasts, where the surface  
60 temperature warming rate was about two or three times faster than that of the global ocean  
61 average for 1970-2020 (e.g., Pershing et al., 2015; Wang et al., 2023).

62 Previous studies have also attributed regional acceleration and spatial variation of the US  
63 East Coast sea level rise to ocean circulation changes, including a weakening of the Gulf Stream  
64 (e.g., Ezer et al., 2013; Ezer, 2015; Goddard et al., 2015; Park and Sweet, 2015; Dong et al.,  
65 2019), warming of the Gulf Stream and the entire subtropical gyre (e.g., Domingues et al., 2018;  
66 Volkov et al., 2019, 2023; Steinberg et al., 2024; Huang et al., 2025), and a slowdown of the  
67 Atlantic Meridional Overturning Circulation (AMOC, e.g., Levermann et al., 2005; Little et al.,  
68 2017, 2019). While progress has been made in understanding ocean conditions off the US East

69 and Gulf Coasts and in the Caribbean Sea, substantial uncertainties still remain regarding future  
70 changes in regional ocean circulation and their sensitivity to greenhouse gas emissions scenarios.  
71 Consequently, it is essential to investigate projected changes in ocean circulation across  
72 scenarios to improve our understanding of future ocean conditions and ecosystem dynamics  
73 across the Northwest Atlantic.

74 Global models, such as General Circulation models (GCMs) and Earth System Models  
75 (ESMs), offer valuable insights into future ocean conditions under various climate scenarios.  
76 However, they are often limited in spatial resolution due to computational constraints and may  
77 face significant uncertainties due to limitations in representing the fine-scale ocean circulation  
78 and thermohaline structures, particularly in coastal regions. Hence, high-resolution, eddy-  
79 resolving ocean models are critical for addressing these limitations, providing improved  
80 representations of historical ocean circulation across multiple timescales and offering more  
81 reliable future projections (e.g., Drenkard et al., 2021). To leverage the benefits of resolving  
82 eddies and shelf-scale circulation while lowering the computational burden, multiple studies  
83 have applied dynamic downscaling techniques to better understand and project regional impacts  
84 of climate change on NWA ocean systems (e.g., Liu et al., 2012, 2015; Alexander et al., 2020;  
85 Shin and Alexander, 2020; Rutherford et al., 2024).

86 By refining the outputs of GCMs/ESMs using high-resolution regional models, dynamical  
87 downscaling can capture finer-scale processes and interactions that are often missed by coarse-  
88 resolution models. For example, the projected weakening of the Loop Current and associated  
89 reduction in warm water transport through the Yucatan Channel are poorly resolved in Coupled  
90 Model Intercomparison Project Phase 5 (CMIP5) and CMIP6 global models, leading to an  
91 overestimation of SST warming over the northern part of the Gulf of America (GoA; a.k.a. Gulf

92 of Mexico) and underestimation of SST warming along the West Florida shelf - an issue better  
93 addressed by high-resolution downscaled models (e.g., Liu et al., 2012, 2015). Similarly,  
94 systematic CMIP model biases in the Gulf Stream representation led to under-estimation of  
95 warming of Northeast U.S. waters associated with future changes in the Gulf Stream path (Saba  
96 et al., 2016).

97 In line with these efforts, the National Oceanic and Atmospheric Administration (NOAA)  
98 Changing Ecosystems and Fisheries Initiative (CEFI) modeling team has developed a high-  
99 resolution regional ocean model - the Modular Ocean Model version 6 at  $1/12^\circ$  horizontal  
100 resolution ( $\sim 8$  km) for the Northwest Atlantic Ocean (MOM6-NWA12; Ross et al., 2023).  
101 MOM6-NWA12 is configured to capture key regional features and simulate ocean dynamics in  
102 the Northwest Atlantic with high fidelity. This model provides a valuable framework for  
103 studying the complex interactions between large-scale processes and local features that govern  
104 both physical and biogeochemical variability in the region. MOM6-NWA12 demonstrates strong  
105 performance in reproducing a broad range of observed physical and biogeochemical conditions  
106 during the hindcast period (1993-2020, Ross et al., 2023). Furthermore, it exhibits skillful  
107 seasonal to decadal forecast capabilities for SST anomalies (SSTAs, Koul et al., 2024; Ross et  
108 al., 2024). However, while MOM6-NWA12 has shown promise for seasonal and decadal  
109 predictions, its potential for multi-decadal (30~100 years) projections remains unexplored.

110 In this study, we use the high-resolution MOM6-NWA12 model to dynamically downscale  
111 future projections from the Geophysical Fluid Dynamics Laboratory's Earth System Model  
112 version 4.1 (GFDL-ESM4.1) for the Northwest Atlantic Ocean. With this downscaling  
113 procedure, we aim to generate more accurate and regionally relevant projections of future ocean  
114 conditions. Unlike prior studies, which used a single greenhouse gas emissions scenario, we

115 consider the range of potential ocean futures from projections using four different scenarios (i.e.,  
116 Shared Socioeconomic Pathways; SSP-126, SSP-245, SSP-375, and SSP-585) spanning  
117 aggressive mitigation to high emissions pathways beyond our current trajectory. This allows us  
118 to identify the NWA responses to future climate change that are sensitive to emissions pathways  
119 from those that are not, and to explore mechanisms underlying these contrasts. We also build on  
120 prior work to understand regional hot-spots of ocean change and their drivers. This approach  
121 enhances our understanding of regional ocean dynamics and supports the development of  
122 effective mitigation and adaptation strategies in response to climate change.

123

## 124 **2. Model and downscaling settings**

### 125 2.1 MOM6-NWA12

126 MOM6-COBALT-NWA12 is a coupled ocean circulation and sea ice model which can also  
127 include coupled ocean biogeochemistry (Ross et al., 2023). Here, we consider a “physics-only”  
128 implementation of this system (i.e., MOM6-NWA12), which has also been applied for seasonal  
129 and decadal prediction applications (Ross et al., 2024; Koul et al., 2024). The model spans the  
130 Northwest Atlantic Ocean, including the Caribbean Sea, the Gulf Coast, and the U.S. East Coast  
131  $98^{\circ}\text{W}$ - $36^{\circ}\text{W}$  and  $5^{\circ}\text{N}$ - $52^{\circ}\text{N}$ , and has  $775 \times 845$  grid points (Fig. 1). The nominal horizontal  
132 resolution is about  $1/12^{\circ}$ . The zonal distance between grid points varies with latitude, from  $\sim 9$   
133 km at the southern boundary to  $\sim 5$  km at the northern boundary. The model has 75 vertical  
134 layers using a  $z^*$ -coordinate, a depth coordinate rescaled with the free surface (Adcroft and  
135 Campin, 2004). The vertical resolution is finest near the surface, where the layer thickness is 2  
136 m, increasing gradually with depth to a maximum thickness of 250 m above the deepest model  
137 depth of 6500 m. The model’s subgrid-scale parameterizations are adapted from the  $1/4^{\circ}$  global

138 MOM6, with updates and modifications to account for the increased horizontal resolution (Ross  
139 et al., 2023). MOM6-NWA12 has the option of using time steps for thermodynamics and ocean-  
140 biogeochemistry longer than the baroclinic time step, which significantly reduces the running  
141 time for coupled model simulations. More detailed model description, additional features, and  
142 parameterization settings can be found in Ross et al. (2023).

143

## 144 2.2 GFDL-ESM4.1

145 NOAA GFDL's Earth System Model version 4.1 (GFDL-ESM4.1, Dunne et al. 2020)  
146 provides the boundary conditions for the MOM6-NWA12 simulations. We carried out four sets  
147 of MOM6-NWA12 simulations downscaling GFDL-ESM4.1 simulations under SSP-126, SSP-  
148 245, SSP-375, and SSP-585 scenarios (O'Neill et al, 2016). GFDL-ESM4.1 is built on a basis of  
149 GFDL's AM4.0 atmospheric model, which has 49 hybrid vertical layers and approximately  $1^\circ \times$   
150  $1^\circ$  horizontal resolution (Zhao et al., 2018a, 2018b), using the Finite Volume version 3 (FV3;  
151 Lin, 2004) dynamical core with advanced parameterizations of moist convection, clouds,  
152 radiation, topographical drag, and several other physical processes from its previous version. The  
153 land model in GFDL-ESM4.1 is GFDL's Land Model version 4.1 (LM4.1; Shevliakova et al.,  
154 2024), which improved radiative properties for vegetation, soil, and snow, and updated  
155 hydrology in LM4.0. The ocean model component of GFDL-ESM4.1 uses MOM6 (Adcroft et  
156 al., 2019), configured with a nominal resolution of  $1/2^\circ$  horizontally and 75 vertical hybrid  $z^*$ -  
157 coordinate layers within the Arbitrary-Lagrangian-Eulerian algorithm (Adcroft & Hallberg,  
158 2006), and the GFDL's Sea Ice Simulator (SIS2; Adcroft et al., 2019). More detailed model  
159 description, additional features, and parameterization settings of GFDL-ESM4.1 can be found in  
160 Dunne et al. (2020). It is noted that the equilibrium climate sensitivity (ECS) of GFDL-ESM4 is

161 approximately 2.6 K, which is at the lower end of the sensitivity range for CMIP6 models  
162 (Dunne et al., 2020; Meehl et al., 2020; Sentman et al., 2026).

163

### 164 2.3 Reanalysis datasets

165 The global reanalysis datasets used to force the retrospective ocean simulation of Ross et al.  
166 (2023) are also used here for bias corrections of ocean lateral boundary conditions, surface  
167 forcings, and river discharge for the historical and future projections derived from GFDL-  
168 ESM4.1 (Table 1). We use the high-resolution ( $1/12^\circ$ ) Global Ocean Physics Reanalysis  
169 (GLORYS12; Lellouche et al., 2021) to derive monthly ocean temperature, zonal and meridional  
170 speeds of ocean current, salinity, and sea surface height (SSH) for 1993-2020 period. We also  
171 use 3-hourly European Centre for Medium-Range Weather Forecast (ECMWF) Reanalysis  
172 version 5 (ERA5) atmospheric reanalysis datasets to derive near-surface zonal and meridional  
173 winds, near-surface air temperature, specific humidity, precipitation, and downwelling short- and  
174 long-wave radiative fluxes (Hersbach et al., 2020).

175 For river discharge, we use the gridded daily Global Flood Awareness System (GloFAS)  
176 version 3.1 reanalysis (Alfieri et al., 2020). Although global river discharge driven by climate  
177 change exhibits a clear positive trend, the projected changes in river discharge in our regional  
178 model domain (i.e., the southern and eastern US seaboards) are insignificant and uncertain  
179 during the first half of the 21st century (Muller et al., 2024). Therefore, we did not consider  
180 future changes in runoff in this single-model downscaling and instead applied the daily mean  
181 climatology (1993–2020) of GloFAS river runoff data for the entire simulation period (1950–  
182 2100). As a result, the potential effects of regional runoff change on nearshore salinity and sea  
183 level are not addressed in this study.

184

185 **Table 1.** Reanalysis products and associated variables used for the bias correction and validation

186 in this study.

Reanalysis product	Variables	Frequency
ERA5	2 m temperature	3 hourly
	2 m specific humidity	3 hourly
	10 m zonal wind	3 hourly
	10 m meridional wind	3 hourly
	Sea level pressure	Daily
	Liquid precipitation rate	Daily
	Snowfall rate	Daily
	Downward shortwave radiative flux	Daily
	Downward longwave radiative flux	Daily
GLORYS12	Sea water potential temperature	Monthly
	Sea water salinity	Monthly
	Sea water zonal velocity	Monthly

	Sea water meridional velocity	Monthly
	Sea surface height	Monthly
GloFAS	River runoff rate	Daily

187

#### 188 2.4 Mean bias correction

189 To reduce systematic biases in the GFDL-ESM4 outputs, we applied a climatological mean  
 190 bias correction to the lateral ocean boundary conditions (BCs) and surface atmospheric forcing  
 191 fields using the GLORYS12 and ERA5 reanalysis datasets as follows:

$$192 \text{ Bias-corrected variables} = \text{GFDL-ESM4} + \text{Delta}$$

$$193 \text{ Delta} = \langle \text{Reanalysis} \rangle - \langle \text{GFDL-ESM4} \rangle$$

194 where the GFDL-ESM4 refers to the raw outputs from the GFDL-ESM4 simulations.

195  $\langle \text{Reanalysis} \rangle$  and  $\langle \text{GFDL-ESM4} \rangle$  are the long-term averaged annual cycles from the reanalysis  
 196 and GFDL-ESM4 simulations for the 1993-2020 period, respectively. For the GFDL-ESM4  
 197 simulations, we merged the data from its historical simulation (1993-2014) with the data from  
 198 the future period in each of the four SSP scenarios (2015-2020). The long-term (1993-2020)  
 199 means for each month of the year determine the mean annual cycle of the ocean variables, while  
 200 the long-term means for each 3-hourly frequency of the year determine the mean annual cycle of  
 201 the atmospheric variables. The mean bias correction terms, Delta, were then added to the GFDL-  
 202 ESM4 outputs for the entire simulation period (1950-2100) to correct the mean biases. This bias  
 203 correction method ensures that mean states of MOM6-NWA12 during the historical period  
 204 (1993-2020) are comparable to those in the reanalysis datasets and in Ross et al. (2023).

205 It is noted that our “Delta method” shares similarities with approaches from previous studies  
206 (Liu et al., 2012; 2015; Alexander et al., 2020; Shin and Alexander, 2020; Pozo-Buil et al.,  
207 2021), which replace model climatology with reanalysis climatology to reduce mean biases.  
208 However, our method fundamentally differs in its treatment of high-frequency atmospheric  
209 forcing. While those previous studies utilized high-frequency atmospheric forcing (i.e., daily  
210 time scales) from historical reanalysis datasets for future projections - thereby assuming that  
211 high-frequency forcing remains unchanged in the future -we retained the model-generated high-  
212 frequency atmospheric variability (e.g., 3-hourly and daily). We took this approach to ensure  
213 more consistent climate projections, recognizing that weather and climate are interdependent.  
214 Indeed, not only does weather depend strongly on low-frequency variability (e.g., weather  
215 conditions during the different phases of ENSO are substantially different), but also weather  
216 statistics can substantially change under future climate conditions (e.g., Cheng et al., 2012;  
217 Jeong and Sushama, 2019).

218 A second notable difference between the methodology herein and past Northwest Atlantic  
219 downscaling studies is the replacement of limited “time slice” experiments with a continuous  
220 integration over the historical and future periods. The continuous integration approach requires  
221 more computational investment (time slices were generally compared across 10-30 year intervals  
222 while continuous integrations required 150 years), but it allows for a more complete analysis of  
223 the emergence of significant differences between scenarios and historical conditions, and  
224 between the scenarios themselves (e.g., Drenkard et al., 2021).

225 Finally, for sea level, we note that both GFDL-ESM4.1 and MOM6-NWA12 utilize the  
226 Boussinesq approximation, which conserves ocean volume. The dynamic sea level in both  
227 models can respond to local density changes driven by local warming and freshening (e.g.,

228 Steinberg et al., 2024). However, these models cannot simulate global mean sea-level (GMSL)  
229 rise caused by thermosteric expansion or added mass from ice melt (e.g., Greatbatch, 1994;  
230 Griffies and Greatbatch, 2012; Griffies et al., 2014). Furthermore, to prevent potential drifts in  
231 the basin-integrated water volume associated with the lateral open boundary conditions, we  
232 explicitly constrain the basin-averaged SSH anomaly to be zero throughout all MOM6-NWA12  
233 simulations. Consequently, the SSH changes derived from MOM6-NWA12 strictly represent the  
234 dynamic redistribution of water mass driven by regional ocean circulation and local steric  
235 adjustments.

236

### 237 **3. Results**

#### 238 3.1. Model validation for the historical period

239 To evaluate the performance of GFDL-ESM4.1 and MOM6-NWA12 in the historical period,  
240 we first compared model-derived climatologies of SST, sea surface salinity (SSS), and surface  
241 current speed against the GLORYS12-derived climatological patterns (Fig. 2 and Supplementary  
242 Fig. S1). The GFDL-ESM4.1 outputs show considerable biases in the SST and SSS mean  
243 patterns. Specifically, the SST has a warm bias  $>3^{\circ}\text{C}$  in the Mid-Atlantic Bight (MAB), and a  
244 cold bias  $>2^{\circ}\text{C}$  in magnitude along the North Atlantic Current path compared to the data-  
245 assimilative GLORYS12 product (Fig. 2d). GFDL-ESM4.1 SSS is saltier than the GLORYS SSS  
246 over the entire domain (Fig. 2e), especially in the MAB and along the US Gulf Coast, where the  
247 bias reaches values  $>3$  PSU. These biases are greatly reduced in the MOM6-NWA12. For  
248 example, the SST biases in the MAB and along the Gulf Stream are  $\sim 1^{\circ}\text{C}$  or lower (Fig. 2g).  
249 The SSS shows a small negative bias, except over the Gulf of Maine, where SSS is  
250 overestimated by about 0.7 PSU (Fig. 2h).

251 The bias patterns for surface ocean velocity reveal that ESM4.1's Loop Current is more  
252 diffusive and extended more northward compared to that in GLORYS12 (Fig. 2f and  
253 Supplementary Fig. S1c). This appears to be due to the coarse horizontal resolution of GFDL-  
254 ESM4.1 ( $\sim 0.5^\circ$ ), which is not fine enough to resolve the Loop Current dynamics (e.g., Liu et al.,  
255 2012; 2015). In addition, ESM4.1's Gulf Stream along the South Atlantic Bight (SAB) is weaker  
256 and slightly shifted away from the US East Coast compared to that in GLORYS12  
257 (Supplementary Fig. S2). In contrast, MOM6-NWA12 shows much improvement of both the  
258 Loop Current and Gulf Stream System (Fig. 2i and Supplementary Fig. S1f). For instance, the  
259 Florida Current (beginning of the Gulf Stream System) in MOM6-NWA12 flows closer to the  
260 coastline compared to that in GFDL-ESM4.1 with speeds exceeding  $1 \text{ m s}^{-1}$ , a pattern similar to  
261 GLORYS12 (Fig. 2f and Fig. 2i).

262 After the separation of the Gulf Stream from the US East Coast, the sluggish flow in GFDL-  
263 ESM4.1 is shifted northward compared to GLORYS12, both at its separation point and as it  
264 travels eastward across the North Atlantic (Fig. 2f). In contrast, the faster Gulf Stream in  
265 MOM6-NWA12 (Fig. 2i) is shifted southward at its separation from the coast before regaining  
266 consistency with the data-assimilative GLORYS12 path to the east. This is more clearly shown  
267 in Supplementary Fig. S2, which shows the position of the Gulf Stream core as a  $15^\circ\text{C}$  isotherm  
268 at 200m (e.g., Sanchez-Franks and Zhang, 2015; Hameed et al., 2018; Seidov et al., 2019; Ross  
269 et al., 2023). A northward shift in the Gulf Stream position is typical in low-resolution ocean  
270 models and has been attributed to misrepresentation of nonlinear vorticity boundary dynamics.  
271 While it is not clear why the Gulf Stream in MOM6-NWA12 is shifted southward, previous  
272 studies have indicated that the separation of the Gulf Stream in an eddy-resolving model is very

273 sensitive to the choices made for subgrid scale parameterizations (e.g., Chassignet and Marshall,  
274 2008).

275 Consistent with the surface current speed and position of the Gulf Stream, GFDL-ESM4.1  
276 displays a large negative bias in the dynamic sea surface height (SSH), immediately south of the  
277 Gulf Stream core and its extension to the North Atlantic Current. Connected with this, the  
278 recirculation gyre south of the Gulf Stream (35°N- 73°W), known as the Worthington Gyre  
279 (Worthington, 1976), is almost completely absent in GFDL-ESM4.1 (Fig. 3b and d). On the  
280 other hand, the spatial pattern of the dynamic SSH in MOM6-NWA12 exhibits improved  
281 agreement with that in GLORYS12 (Fig. 3c and e), reproducing a Worthington Gyre albeit  
282 weaker than GLORYS12. Given that the Worthington Gyre is a long-term mean rectification of  
283 the Gulf Stream rings and instability waves not resolved at coarse resolution, it is not surprising  
284 that the recirculation gyre is better represented in MOM6-NWA12 while it is nearly absent in  
285 GFDL-ESM4.1.

286 Lastly, we evaluated the volume transports of Northwestern Atlantic boundary current  
287 systems across four zonal transects for the Yucatan Current, Florida Current, Antilles Current,  
288 and the Deep Western Boundary Current (DWBC), which are key components of AMOC  
289 (McCarthy et al., 2015), as shown in Fig. 4. The zonal transection lines for the four current  
290 systems are shown in Fig. 1 (red solid lines). The Antilles Current transport was obtained by  
291 integrating the meridional flow over the upper 500 m across 26.5°N and 77.5°W-75°W.  
292 Similarly, the DWBC transport was obtained by integrating the meridional velocity between  
293 1,000m and 5,000m across 26.5°N and 77.5°W-75°W. GFDL-ESM4.1 simulates a Yucatan  
294 Current transport of  $43.9 \pm 2.87$  Sv, which is about 62% larger than in-situ observation of  $27.5 \pm$   
295  $2.6$  Sv (Athié et al., 2020, Fig. 4a). In contrast, MOM6-NWA12 simulates a transport of  $24.2 \pm$

296 1.7 Sv, which agrees much better with the observed transport. However, the Florida Current  
297 (80°W-77.5°W) transport simulated by MOM6-NWA12 ( $24.3 \pm 1.6$  Sv) underestimates the  
298 observation ( $32.5 \pm 3.2$  Sv in Volkov et al., 2024), whereas the Florida Current transport  
299 simulated by GFDL-ESM4 ( $34.4 \pm 2.5$  Sv) is comparable to the observation. This occurs despite  
300 far more realistic surface current speeds in MOM6-NWA12 (i.e., Fig. 2f and i) because the  
301 ESM4.1 Florida Current is far more diffuse and extends to greater depth. Additional sensitivity  
302 simulations indicate that the Florida Current transport in MOM6-NWA12 is quite sensitive to the  
303 eddy viscosity (not shown). By increasing the model diffusivities in MOM6-NWA12, the  
304 simulated Florida Current transport also increased closer to the observed value. However, this  
305 occurred at the expense of other model features, such as the latitude of Gulf Stream separation  
306 from the coast, becoming less realistic. Therefore, the momentum and density diffusivities for  
307 MOM6-NWA12 are unchanged from those used in Ross et al. (2023).

308 As shown in Fig. 4c and d, the simulated transports for both the Antilles Current ( $12.3 \pm 4.1$   
309 Sv) and the DWBC ( $-20.8 \pm 8.8$  Sv) in the GFDL-ESM4.1 show substantial disagreement with  
310 observations ( $4.7 \pm 5.2$  Sv for the Antilles Current, Meinen et al., 2019; and  $-31.2 \pm 5.5$  Sv for  
311 the DWBC, Zantopp et al., 2017). MOM6-NWA12, in contrast, better reproduced both the  
312 Antilles Current ( $3.4 \pm 5.6$  Sv) and the DWBC ( $-35.2 \pm 9.5$  Sv). The large biases in GFDL-  
313 ESM4.1 appear to be linked to the overly diffusive and broad Antilles Current and DWBC  
314 (Supplementary Fig. S3).

315 Overall, the high-resolution MOM6-NWA12 configuration generally shows large  
316 improvement in simulating regional ocean circulation and mean conditions compared to the low-  
317 resolution GFDL-ESM4.1. Some deficiencies, however, still exist. Potential impacts of these

318 deficiencies on projected changes, and pathways for future model improvement, will be  
319 discussed in Section 4.

320

## 321 3.2. Future projections

### 322 3.2.1. SST and SSS

323 We first examine the projected spatial changes in SST and SSS derived from the MOM6-  
324 NWA12, comparing the historical period (HIST: 1993–2020) with the late 21st century (L21C:  
325 2073–2100) across four SSP scenarios (SSP-126, SSP-245, SSP-370, and SSP-585). MOM6-  
326 NWA12 shows that SST changes in the future exhibit basin-wide warming with discernable end-  
327 of-century differences (Fig. 5a-e). The domain-averaged SST warming is lowest in the SSP-126  
328 (0.52 °C) simulation and intensifies progressively in SSP-245 (1.21 °C), SSP-370 (1.86 °C) and  
329 SSP-585 (2.23 °C) simulations. The SST increase is particularly large in the MAB, the Gulf of  
330 Maine, and around the Georges Bank. Temperatures are projected to warm by 4°C in some areas  
331 in the SSP-585 scenario (Fig. 5e). Warming in these regions around the MAB and the Gulf of  
332 Maine (35°N–42°N, 75°W–60°W) is reduced to ~3°C, ~2°C and ~1°C in SSP-370, SSP-245 and  
333 SSP-126, respectively (Fig. 5b-d). Mean warming over the next 30 years (2025-2055), is  
334 expected to ~1-2°C with less separation between scenarios (Supplementary Fig. S4).

335 Similar to the SST change, the amplitude of the SSS change is sensitive to the SSP scenarios  
336 (Fig. 5f-j). The increase in domain-averaged SSS is more pronounced in the higher emission  
337 scenarios (0.13 PSU for SSP-126, 0.22 PSU for SSP-245, 0.41 PSU for SSP-370, and 0.46 PSU  
338 for SSP-585). While SSS tends to increase in the subtropical part of the domain, the largest  
339 projected SSS increase is along the SAB, the continental slope off the MAB and the West

340 Florida Shelf where the future change intensifies progressively under the high-emission  
341 scenarios.

342 The large increases in SST and SSS on the West Florida Shelf and the SAB appear to be  
343 linked to the projected weakening of the Loop Current and Gulf Stream (Fig. 6). Additionally,  
344 the weakening of the Gulf Stream leads to a northward shift after its separation from the US East  
345 Coast in the late 21st century in all four SSP scenarios (Fig. 6, Section 3.2.2), consistent with  
346 previous studies (e.g., Saba et al., 2016; Caesar et al., 2018; Bellomo et al., 2021). It appears that  
347 the SST increase along the edge of the MAB is linked to the northward shift of the Gulf Stream  
348 and the implied warm water intrusion to the Slope Sea (Saba et al., 2016). Warming via this  
349 mechanism is fortified by commensurate mean reductions of the advection of cold high-latitude  
350 waters from the Labrador Sea as described further in the Discussion section. Interestingly, a  
351 narrow region of minimal surface warming is evident immediately south of the historical Gulf  
352 Stream path around 35 °N, 60°W (Fig. 6e). A similar, but smaller area of minimum surface  
353 warming is also evident in the northern GoA, which is largely consistent with previous studies  
354 (Liu et al., 2012, 2015). These regions of minimal SST warming appear to be linked to the  
355 reduced Gulf Stream or the reduced Loop Current, implying a reduction in ocean heat  
356 convergence to these regions (Figs. 6e and 6i).

357 While GFDL-ESM4.1 shows the SSP scenario sensitivity for the amplitude of the future SST  
358 and SSS changes, the pronounced SST warming identified by MOM6-NWA12 in the Mid-  
359 Atlantic Bight (MAB) and Gulf of Maine regions is much reduced in GFDL-ESM4.1 (Fig. 7).  
360 This is consistent with the absence of a future northward shift in the Gulf Stream in the coarse  
361 resolution GFDL-ESM4.1 (Fig. 8) and prior findings of Saba et al., (2015).

362 In summary, MOM6-NWA12 projections of SST, SSS, and surface current speed indicate  
363 that under all four future scenarios, the Northwestern Atlantic basin becomes significantly  
364 warmer, and saltier especially along the US East Coast and the West Florida shelf regions, and  
365 the Gulf Stream becomes considerably weaker and shifts northward. The magnitude of projected  
366 end-of-century changes, however, varies considerably across scenarios. Most notably, the  
367 severity of the impacts projected by the prior worst-case scenario in CMIP5 (i.e., SSP-585) are  
368 progressively mitigated by lower emissions scenarios. Differences between scenarios, however,  
369 are far smaller in the first half of the century.

370

### 371 3.2.2. WBC transports

372 As shown in Figs. 6, the entire WBC system, including the North Brazil Current, Caribbean  
373 Current, Yucatan Current, Loop Current, Florida Current, and the Gulf Stream, weakens, at least  
374 at the surface, consistent with previous future projection studies (e.g., Liu et al., 2012, 2015;  
375 Saba et al, 2016; Alexander et al., 2020; Shin and Alexander, 2020; Beadling et al., 2018;  
376 Roberts et al., 2019). The regions of minimal SST warming appear to be linked to the reduced  
377 Gulf Stream or the reduced Loop Current, implying a reduction in ocean heat convergence to  
378 these regions (Figs. 6e and 6i). To further explore volume transport by the WBCs system, we  
379 examine the temporal changes in the volume transport in the Florida Current, Yucatan Current,  
380 Antilles Current, and the Deep Western Boundary Current (DWBC), as shown in Fig. 9.

381 The Florida Current exhibits a gradual decline throughout the 21st century across all SSP  
382 scenarios. The largest decrease in the late 21st century is shown in the SSP-585 scenario (Fig.  
383 9a), from  $24.2 \pm 1.7$  Sv in the historical period to  $15.2 \pm 3.5$  Sv in the late 21st century (37.2 %  
384 decline) while the smallest decrease in the late 21st century is shown in the SSP-126 scenario

385 (24.3% decline). The intermediate cases more consistent with current CO<sub>2</sub> trajectories also  
386 exhibit smaller shifts than the prior worst case. The Yucatan Current shows similar rates of  
387 decrease and scenario sensitivity. Under SSP-585, the Yucatan Current transport decreased from  
388  $21.0 \pm 2.1$  Sv in the historical period to  $13.2 \pm 3.1$  Sv in the late 21st century (37.1 % decline,  
389 Fig. 9b) but end-of-century declines are partially mitigated at intermediate and low emissions  
390 cases. The mean transport by the Antilles Current is significantly reduced from  $3.4 \pm 5.6$  Sv in  
391 the historical period to  $-0.72 \pm 4.5$  Sv in the late 21st century, under SSP-585, with relatively  
392 weak variation across scenarios. This suggests that the Antilles Current may disappear (nearly  
393 zero mean transport) after around 2080 (Fig. 9c). This weakening (and the reversal) of the  
394 Antilles Current, which is consistent with a previous modeling study (Cai et al., 2024), may play  
395 a key role in the subtropical gyre recirculation and the upper-ocean stratification in the SAB. Fig.  
396 9d shows that volume transport of the Deep Western Boundary Current (DWBC), which is a  
397 vital return flow component of the AMOC from the high latitudes, exhibits the strongest  
398 response to anthropogenic warming. Particularly under the SSP-585 scenario, the DWBC  
399 transport declines from  $-35.2 \pm 9.5$  Sv in the historical period to  $-20.2 \pm 16.0$  Sv in the late 21st  
400 century (42.7 % decline), reflecting a substantial slowdown in the AMOC under SSP-585 (Fig.  
401 10). This slowdown is once again mitigated in part by intermediate and low emissions scenarios.

402 As was the case for SST, SSS and current speed, the rate of weakening was not very sensitive  
403 to the emission scenarios before the 2070s. Similarly, the time series of volume transports in the  
404 WBCs system shows a similar rate of decline across all four SSP scenarios until approximately  
405 2070 (Fig. 9). The insensitivity of Northwestern Atlantic WBCs to emission scenarios before  
406 2070s is consistent with the AMOC decline in GFDL-ESM4.1, given that the WBCs are key  
407 contributors to the AMOC (Fig. 10). Previous studies (e.g., Weijer et al., 2020; Baker et al.,

408 2023) found that the rate of AMOC weakening derived from most CMIP6 models shows limited  
409 sensitivity to emission scenarios prior to around 2070, consistent with GFDL-ESM4.1. It is  
410 important to note that the greenhouse gas forcings for the CMIP6 SSP scenarios begin to diverge  
411 after the historical period (~2014), with separation in their radiative forcing pathways emerging  
412 by the mid-21st century. The results that WBC volume transports and AMOC remain relatively  
413 insensitive to these diverging emissions scenarios for several decades provides critical evidence  
414 for a delayed ocean response to greenhouse gas forcing.

415

### 416 3.2.3. Dynamic SSH

417 We next explore dynamic SSH and its projected changes under four SSP scenarios (Fig. 11).  
418 Substantial changes in both the amplitude and spatial pattern of dynamic SSH are projected in  
419 the Northwestern Atlantic. In particular, dynamic SSH increases greatly along the West Florida  
420 Shelf (WFS), SAB, MAB, and Georges Bank, and decreases immediately south of the Gulf  
421 Stream (after its separation from the US East Coast) under all four SSP scenarios (Fig. 11).  
422 Given that these changes are largely confined to the region of WBCs and the southern  
423 recirculation (or Worthington) gyre south of the Gulf Stream, the dynamic SSH changes appear  
424 to be directly linked to the substantial weakening of the WBC system (e.g., the Loop Current, the  
425 Florida Current, and the Gulf Stream) and the implied relaxation of the thermocline slope (i.e., a  
426 redistribution of mass) across the WBCs. The projected increases in dynamic SSH along the  
427 WFS, SAB, MAB, and the Georges Bank appear to be largely driven by the AMOC weakening  
428 (e.g., Yin et al., 2009; Little et al., 2017; Weijer et al., 2020). Note that the dynamic SSH  
429 changes in these regions can be also modulated by the future change in the wind-driven gyre  
430 circulation, which is not explicitly isolated and evaluated in this study.

431 Consistent with MOM6-NWA12, GFDL-ESM4.1 shows an increase in dynamic SSH near  
432 the U.S. East Coast and decreases south of the Gulf Stream (after its separation from the US East  
433 Coast) in the late 21st century (Fig. 12). An interesting point to note is that MOM6-NWA12  
434 projects a stronger SSH increase in the SAB than in the MAB while GFDL-ESM4.1 projects a  
435 stronger SSH increase over the MAB than in the SAB. Consistent with this result, Li et al. (2022)  
436 show that the projected SSH derived from a high-resolution Community Earth System Model  
437 (CESM) increases more in the SAB than in the MAB, while that derived from a low-resolution  
438 CESM increases more in the MAB than in the SAB.

439 To further explore the future increases in dynamic SSH along the US South and East Coasts,  
440 we examine the projected dynamic SSH changes over the continental shelf (i.e., depths < 200m)  
441 for five sub-regions, namely the Northern GoA, WFS, SAB, MAB, and Gulf of Maine, as shown  
442 in Fig. 13. The future increase in dynamic SSH is relatively modest in the Northern GoA and  
443 WFS, ranging between 5 and 7 cm during the mid- and late-21st century (2041-2100). These  
444 increases occur mainly during the mid-21st century (2041-2060), after which there is no  
445 significant increase in the dynamic SSH in these shelf regions. Another important feature is that  
446 the dynamic SSH increases in the GoA and WFS (Figs. 13a-b) are not sensitive to the emission  
447 scenarios considered. Given that the dynamic SSH increase in these regions is mainly driven by  
448 the projected weakening of the AMOC and the associated Loop Current, this result appears to be  
449 consistent with the insensitivity in the rate of AMOC's future weakening to the emission  
450 scenarios prior to 2070 (Fig. 10).

451 In contrast to the Northern GoA and WFS, the projected dynamic SSH changes in the US  
452 East Coast shelf regions (i.e., SAB, MAB, and Gulf of Maine) are significantly larger, ranging  
453 between 10 and 20 cm in the late-21st century. Additionally, unlike the US GoA shelf regions

454 (i.e., Northern GoA and WFS), the increase in dynamic SSH in these regions continues beyond  
455 the mid-21st century to the late-21st century, implying that the weakening of the AMOC and the  
456 associated WBCs have much tighter control over these regions. A systematic tendency toward  
457 greater dynamic SSH changes in higher emissions scenarios also begins to emerge after 2070,  
458 though there is still significant variation around this trend (e.g., SSP-370 has a lower local  
459 dynamic sea level change than SSP245 despite having higher emissions), presumably due to  
460 internal climate variability.

461 Among the five sub-regions considered, the dynamic SSH change in the SAB is subject to  
462 the largest increase. The dynamic SSH in the SAB is projected to increase dramatically after  
463 around 2040, reaching close to 20 cm in the late 21st century compared to that in the historical  
464 period. This suggests that the SAB is the most sensitive to the projected slowdown of the AMOC  
465 and the WBCs in MOM6-NWA12. Specifically, as shown in Fig. 14, a strong negative  
466 correlation exists between the Florida Current transport and the SAB dynamic SSH (e.g., Ezer,  
467 2019; Ezer and Atkinson, 2014) indicating that a -1 Sv reduction in the Florida Current transport  
468 corresponds to about 1.7 cm of dynamic SSH increase in the SAB. This indicates that the SAB is  
469 the future dynamic SSH rise hotspot, potentially posing an increasing flooding risk in the coastal  
470 communities. This appears to be partly due to close proximity of the SAB to the WBC (i.e.,  
471 Florida Current in this case). In the other subregions, the shelf area is too far away from the  
472 WBC (Northern GoA), too wide (WFS), or mediated by the slope water (MAB and Gulf of  
473 Maine).

474 To better understand the relationship between the SAB dynamic SSH increase and the Gulf  
475 Stream weakening, we show the vertical profile of ocean temperature and salinity across 26.5°N  
476 during the historical period and their projected changes under the four SSP scenarios (Fig. 15).

477 Fig. 15 clearly illustrates a substantial warming and an increase in salinity, mainly along the  
478 continental slope and shelf. A distinct decrease in density (i.e., lighter water) emerges on the  
479 western side of the Florida Current around 200 m depth (Supplementary Fig. S5). This localized  
480 density reduction reflects a relaxation, or flattening, of the upward-tilted isopycnals along the  
481 Florida coast. Consequently, this flattening of the isopycnals weakens the cross-stream  
482 horizontal density gradient, thereby reducing northward volume transport in the Florida Straits.  
483 Due to reduced bottom Ekman transport and a relaxation, or a flattening, of the upward-tilted  
484 isopycnals associated with a weakened Gulf Stream, upwelling decreases along the continental  
485 slope and shelf, limiting the supply of cold and relatively fresh subsurface water from underneath  
486 the Gulf Stream. This indicates that the warm and salty Gulf Stream water penetrates deeper into  
487 the continental slope and shelf region due to the weakening of the Gulf Stream. This baroclinic  
488 mass redistribution between the open ocean and the coastal region is also directly responsible for  
489 the large projected increase in dynamic SSH across the SAB, which is consistent with the  
490 historical analysis of Steinberg et al. (2024). These future changes in ocean conditions near the  
491 coastline are also projected in West Florida. The reduction of the Loop Current leads to an  
492 increase in dynamic SSH across West Florida and a significant reduction in the upwelling of cold  
493 and relatively fresh subsurface water. This, in turn, results in warm, salty Loop Current water  
494 penetrating deeper into the WFS (Fig. 16).

495 In the MAB (30°N–41°N, 76°W–67°W), the weakening and shoreward shift of the Gulf  
496 Stream in the late 21st century drives an increase in ocean temperature and salinity along the  
497 continental slope and shelf (Fig. 17). The maximum SSH anomaly is observed near the core  
498 location of the shifted Gulf Stream. Specifically, projected SSH increases on the coastal side of

499 the current while decreasing on the open-ocean side. This differential change results in a reduced  
500 cross-stream SSH gradient (slope), consistent with the geostrophic weakening of the flow.

501 Finally, we emphasize that the dynamical SSH changes driven by changes in ocean currents  
502 would occur in addition to the GMSL rise associated with ocean warming and glacial and ice-  
503 sheet melt. As described in the methods, MOM6-NWA12 can respond to local density changes  
504 driven by local warming and freshening (e.g., Steinberg et al., 2024), even though GMSL rise is  
505 not directly reflected in the model simulation due to the Boussinesq approximation. Therefore, to  
506 explore the total coastal SSH change (i.e., dynamic SSH changes plus GMSL rise) in the late  
507 21st century, the dynamic SSH changes derived from MOM6-NWA12 are combined with the  
508 projected GMSL change. According to the IPCC AR6 report (IPCC, 2021), the projected GMSL  
509 rise by the late 21st century relative to the historical period is 0.38 m for SSP-126, 0.47 m for  
510 SSP-245, 0.56 m for SSP-370, and 0.64 m for SSP-585, respectively. Specifically, in the SAB  
511 under the SSP-585 scenario, the dynamic sea level increase by the late 21st century (~0.2 m)  
512 accounts for nearly 25% of the total sea level increase. This highlights that the SAB could  
513 experience extreme and compounding (e.g., high tides and storm surges) coastal flooding risks in  
514 the future.

#### 515 **4. Summary and Discussion**

516 This study describes and evaluates the dynamically downscaled physics-only MOM6-  
517 NWA12 simulations of GFDL-ESM4, and then explores future changes of the Northwest  
518 Atlantic Ocean under four CMIP6 emission scenarios (SSP-126, SSP-245, SSP-370, and SSP-  
519 585). Validation of model outputs against direct ocean observational and reanalysis data shows  
520 that the biases in GFDL-ESM4 are significantly reduced in MOM6-NWA12, particularly in the  
521 spatial SST and SSS patterns, as well as the Gulf Stream's path and volume transport. For

522 instance, while GFDL-ESM4 exhibits pronounced warm and high salinity biases along the US  
523 East Coast and a northward shift of the Gulf Stream, MOM6-NWA12 simulates improved  
524 representation of these key features, including a better alignment of the Gulf Stream path with  
525 observations. Furthermore, MOM6-NWA12 captures the spatial pattern of SSH much more  
526 accurately, as well as the WBCs (i.e., Florida Current, Yucatan Current, Antilles Current, and  
527 DWBC).

528 The projections derived from MOM6-NWA12 show significant changes in SST, SSS and the  
529 WBCs under the four SSP scenarios considered. The magnitude of end-of-century changes is  
530 strongly scenario-dependent: pronounced SST warming in the MAB and Gulf of Maine,  
531 exceeding 4°C in some areas, emerges as a distinct feature of the prior “worst-case” high-  
532 emission scenarios (SSP-585), partial mitigation is apparent in intermediate trajectories more  
533 consistent with current CO<sub>2</sub> trajectories (SSP-370, SSP-245), and this signal remains modest  
534 under low-emission scenarios (SSP-126). The amplified warming and salinification along the US  
535 South and East Coasts appears to be linked to a weakening of the Loop Current and Gulf Stream  
536 (e.g., Liu et al., 2012, 2015; Saba et al., 2016) alongside a shoreward and northward shift of the  
537 Gulf Stream following its separation from the coast (e.g., Yin et al., 2009; Saba et al., 2016;  
538 Bellomo et al., 2021; Li et al., 2022). In addition, as discussed in New et al. (2021), the MAB  
539 and the Gulf of Maine are also strongly influenced by the Labrador Current and the Labrador  
540 Slope Water (LSLW). The Slope Current in MOM6-NWA12 shows a large bias in its position  
541 and the strength along the MAB. More specifically, it is much weaker compared to that in  
542 GLORYS12, and is replaced by northward flow in the upper 400m or so (Fig. 18). Another core  
543 of southward flow appears immediately shoreward of the Gulf Stream in MOM6-NWA12. Since  
544 it is positioned away from the continental slope (near 73°W), it is referred to as the northern

545 recirculation flow of the Gulf Stream. In the future scenarios, both the northern recirculation  
546 flow and the Slope Current (below 600m) drastically weaken. The Gulf Stream also weakens and  
547 its core shifts shoreward. In the SSP370 and SSP585 scenarios, the Gulf Stream core is  
548 positioned along the continental slope. Thus, both the northern recirculation flow and the Slope  
549 Current (below 600m or so) completely disappear in those high emission scenarios. Therefore,  
550 despite a large bias in the location and strength of the Slope Current in MOM6-NWA12, we can  
551 still conclude that the future warming and saltening in the MAB, shown in Fig. 17, are the result  
552 of a compounding effect - a weakening and shoreward shift of the Gulf Stream combined with  
553 reduced advection of cold, fresh Labrador Sea waters.

554 A consistent feature across all projections is the significant deceleration of the surface speed  
555 and volume transport of the four WBCs (i.e., Yucatan Current, Florida Current, Antilles Current  
556 and DWBC), which aligns well with the significant weakening of the AMOC. Reductions in the  
557 meridional transports of the four WBCs remain insensitive to emission scenarios until the 2070s,  
558 after which they diverge significantly (ranging from ~23% in SSP-126 to ~38% in SSP-585  
559 scenarios).

560 The projections also suggest that the slowdown of the WBCs leads to an increase in dynamic  
561 SSH along the US South and East Coasts, which is largest in the SAB. The increased dynamic  
562 SSH in these regions is directly related to the weakening of the WBCs and the associated  
563 redistribution of the mass across the WBCs (Minobe et al., 2017). As such, a strong negative  
564 correlation exists between the Florida Current transport and the dynamic SSH in the SAB, for  
565 example. Further analysis shown in Fig. 15 indicates that the weakening of the Florida Current  
566 accompanies a substantial reduction of upwelling of cold and fresh subsurface water to the  
567 continental slope and shelf region. The associated decrease in nutrient supply, implied by the

568 reduced upwelling, has important implications for the marine ecosystems and productivity in the  
569 SAB, as the Gulf Stream-induced upwelling represents the main source of nutrients to the SAB  
570 outer and mid shelf (e.g., Lee et al., 1991; Gomez et al., 2026).

571 While this study has mostly focused on describing the future mean changes across scenarios,  
572 there are several areas that require further investigation, such as the changes in the seasonal  
573 circulation patterns and their impact on the anomalous ocean conditions. This could be relevant,  
574 for example, in the MAB where seasonal changes in wind stress drive the annual sea level height  
575 variability (e.g., Yang and Chen, 2025). It could also be relevant for the SAB where the seasonal  
576 wind stress changes impact coastal temperature and cross-shore interchanges through upwelling  
577 (e.g., Castelao et al., 2011; Yuan et al., 2017). Therefore, further study is needed to explore  
578 future changes in the seasonality of WBCs, and their impacts.

579 Lastly, building on these results derived from physics-only simulations, we plan to couple the  
580 physical ocean model with the Carbon, Ocean Biogeochemistry and Lower Trophics (COBALT,  
581 Stock et al., 2020, 2025) model to explore future changes in ocean ecosystems in the Northwest  
582 Atlantic. Additionally, we will expand the scenario-focused ensemble presented here to include  
583 multiple GCMs to fully assess the potential range of the future changes in the Northwest  
584 Atlantic.

585

## 586 **Acknowledgements**

587 We would like to sincerely thank two anonymous reviewers for their thorough reviews and  
588 thoughtful comments and suggestions, which led to a significant improvement of the paper. We  
589 also thank Liz Drenkard for helpful comments and suggestions. This study was supported by the  
590 NOAA's Changing Ecosystems, and Fisheries Initiative (CEFI) and the NOAA award Number

591 NA24OARX405C0044-T1-01. This study was also carried out under the auspices of the  
592 Cooperative Institute for Marine and Atmospheric Studies (CIMAS) (NOAA cooperative  
593 agreement NA20OAR4320472), the Northern Gulf Institute (NGI) (NOAA cooperative  
594 agreement NA21OAR4320190), and supported by NOAA’s Oceanic and Atmospheric Research  
595 and NOAA’s Atlantic Oceanographic and Meteorological Laboratory.

596

### 597 **Code availability**

598 The source code for each component of the MOM6-NWA12 model has been archived by  
599 Ross et al. (2023) and the GitHub repositories are located at [https://github.com/NOAA-](https://github.com/NOAA-GFDL/CEFI-regional-MOM6)  
600 [GFDL/CEFI-regional-MOM6](https://github.com/NOAA-GFDL/CEFI-regional-MOM6). All codes for analyses were performed using the Grid Analysis  
601 and Display System (GrADS), which is publicly available from the Center for Ocean-Land-  
602 Atmosphere Studies at <http://cola.gmu.edu/grads> and NCL, which is publicly available from the  
603 NCAR Command Language (NCL) at <https://www.ncl.ucar.edu/>. The GrADS, NCL, and Fortran  
604 codes used to perform the analyses can be accessed upon request to D. K.

605

### 606 **Data availability**

607 The model outputs derived from the MOM6-NWA12 future projections under four SSP  
608 scenarios will be available at CEFI portal soon ([https://psl.noaa.gov/cefi\\_portal/](https://psl.noaa.gov/cefi_portal/)). GLORYS12  
609 reanalysis dataset is available at <https://data.marine.copernicus.eu/product/>. ERA5 reanalysis  
610 dataset is available at <https://cds.climate.copernicus.eu/datasets/reanalysis-era5-single-levels>.  
611 GFDL-ESM4 outputs are freely available at the CMIP6 archive  
612 (<https://aims2.llnl.gov/search/cmip6/>).

613

614 **Author Contribution**

615 D Kim, AC Ross, SI Shin and SK Lee contributed source code for the downscaling system for  
616 the regional MOM6. D Kim, SI Shin and SK Lee contributed to preparation of model input files.  
617 D Kim, FA Gomez and SK Lee contributed to evaluation and interpretation of the model results.  
618 D Kim and SK Lee prepared the initial draft of the manuscript. All coauthors participated in  
619 discussions during various stages of the model development and evaluation and read and  
620 approved the final version of the manuscript.

621

622 **Competing interests**

623 Dr. Charles A. Stock (one of co-authors) serves as editor for the special issue to which this paper  
624 belongs.

625

626 **References**

- 627 1. Adcroft, A., Anderson, W., Balaji, V., Blanton, C., Bushuk, M., Dufour, C. O., Dunne, J. P.,  
628 Griffies, S. M., Hallberg, R., Harrison, M. J., Held, I. M., Jansen, M. F., John, J. G., Krasting,  
629 J. P., Langenhorst, A. R., Legg, S., Liang, Z., McHugh, C., Radhakrishnan, A., Reichl, B. G.,  
630 Rosati, T., Samuels, B. L., Shao, A., Stouffer, R., Winton, M., Wittenberg, A. T., Xiang, B.,  
631 Zadeh, N., and Zhang, R.: The GFDL Global Ocean and Sea Ice Model OM4.0: Model  
632 Description and Simulation Features, *Journal of Advances in Modeling Earth Systems*, 11,  
633 3167–3211, <https://doi.org/10.1029/2019MS001726>, 2019.
- 634 2. Adcroft, A., and Campin, J.-M.: Rescaled height coordinates for accurate representation of  
635 free-surface flows in ocean circulation models, *Ocean Modelling*, 7, 269–284,  
636 <https://doi.org/10.1016/j.ocemod.2003.09.003>, 2004.

- 637 3. Adcroft, A., and Hallberg, R.: On methods for solving the oceanic equations of motion in  
638 generalized vertical coordinates, *Ocean Modelling*, 11, 224–233,  
639 <https://doi.org/10.1016/j.ocemod.2004.12.007>, 2006
- 640 4. Alexander, M. A., and Scott, J. D.: The Role of Ekman Ocean Heat Transport in the Northern  
641 Hemisphere Response to ENSO, *Journal of Climate*, 21, 5688–5707,  
642 <https://doi.org/10.1175/2008JCLI2382.1>, 2008.
- 643 5. Alexander, M. A., Shin, S., Scott, J. D., Curchitser, E., and Stock, C.: The Response of the  
644 Northwest Atlantic Ocean to Climate Change, *Journal of Climate*, 33, 405–428,  
645 <https://doi.org/10.1175/JCLI-D-19-0117.1>, 2020.
- 646 6. Alfieri, L., Lorini, V., Hirpa, F. A., Harrigan, S., Zsoter, E., Prudhomme, C., and Salamon,  
647 P.: A Global Streamflow Reanalysis for 1980–2018, *Journal of Hydrology*, 6, 100049,  
648 <https://doi.org/10.1016/j.hydroa.2019.100049>, 2020.
- 649 7. Athié, G., Sheinbaum, J., Leben, R., Ochoa, J., Shannon, M. R., and Candela, J.: Interannual  
650 variability in the Yucatan Channel flow, *Geophysical Research Letters*, 42, 1496–1503,  
651 [doi:10.1002/2014GL062674](https://doi.org/10.1002/2014GL062674), 2015.
- 652 8. Baker, J. A., Bell, M. J., Jackson, L. C., Renshaw, R., Vallis, G. K., Watson, A.J., and Wood,  
653 R. A.: Overturning pathways control AMOC weakening in CMIP6 models. *Geophysical  
654 Research Letters*, 50, e2023GL103381. <https://doi.org/10.1029/2023GL103381>, 2023.
- 655 9. Bell, R. J., Richardson, D. E., Hare, J. A., Lynch, P. D., and Fratantoni, P. S.: Disentangling  
656 the effects of climate, abundance, and size on the distribution of marine fish: an example  
657 based on four stocks from the Northeast US shelf, *ICES Journal of Marine Science*, 72,  
658 1311–1322, <https://doi.org/10.1093/icesjms/fsu217>, 2015.

- 659 10. Beadling, R. L., Russell, J. L., Stouffer, R. J. & Goodman, P. J.: Evaluation of subtropical  
660 North Atlantic Ocean circulation in CMIP5 models against the observational array at 26.5°N  
661 and its changes under continued warming. *Journal of Climate*. 31, 9697-9718,  
662 <https://doi.org/10.1175/jcli-d-17-0845.1>, 2018.
- 663 11. Bellomo, K., Angeloni, M., Corti, S. and Hardenberg, J.: Future climate change shaped by  
664 inter-model differences in Atlantic meridional overturning circulation response, *Nature*  
665 *Communications*, 12, 3659, <https://doi.org/10.1038/s41467-021-24015-w>, 2021.
- 666 12. Caesar, L., Rahmstorf, S., Robinson, Feulner, G., and Saba, V.: Observed fingerprint of a  
667 weakening Atlantic Ocean overturning circulation, *Nature*, 556, 191–196,  
668 <https://doi.org/10.1038/s41586-018-0006-5>, 2018.
- 669 13. Cai, J., Yang, H., Chen, Z., and Wu. L.: The disappearing Antilles Current dominates the  
670 weakening meridional heat transport in the North Atlantic Ocean under global warming,  
671 *Environmental Research Letters*, 19, 044049, <https://doi.org/10.1088/1748-9326/ad3567>,  
672 2024.
- 673 14. Castelao, R.: Intrusions of Gulf Stream waters onto the South Atlantic Bight shelf, *Journal of*  
674 *Geophysical Research: Oceans*, 116, C10011, <https://doi.org/10.1029/2011JC007178>, 2011.
- 675 15. Chassignet, E., and Marshall. D.: Gulf Stream separation in numerical ocean models, In  
676 *Ocean Modeling in an Eddy Regime*, *Geophysical Monograph Series*, 177, 2008.
- 677 16. Cheng, C. S., Li, G., Li, Q., Auld, H., and Fu, C.: Possible Impacts of Climate Change on  
678 Wind Gusts under Downscaled Future Climate Conditions over Ontario, Canada, *Journal of*  
679 *Climate*, 25, 3390–3408, <https://doi.org/10.1175/JCLI-D-11-00198.1>, 2012.
- 680 17. Dong, S., Baringer, M., and Goni, G.: Slowdown of the Gulf Stream during 1993–2016.  
681 *Scientific Reports*, 9, 6672, <https://doi.org/10.1038/s41598-019-42820-8>, 2019.

- 682 18. Domingues, R., Goni, G., Baringer, M., and Volkov, D.: What caused the accelerated sea  
683 level changes along the U.S. East Coast during 2010-2015?, *Geophysical Research Letters*,  
684 45, 13367–13376, <https://doi.org/10.1029/2018GL081183>, 2018.
- 685 19. Drenkard, E. J., Stock, C., Ross, A. C., Dixon, K. W., Adcroft, A., Alexander, M., Balaji, V.,  
686 Bograd, S. J., Butenschön, M., Cheng, W., Curchitser, E., Lorenzo, E. D., Dussin, R.,  
687 Haynie, A. C., Harrison, M., Hermann, A., Hollowed, A., Holsman, K., Holt, J., Jacox, M.  
688 G., Jang, C. J., Kearney, K. A., Muhling, B. A., Buil, M. P., Saba, V., Sandø, A. B.,  
689 Tommasi, D., and Wang, M.: Next-generation regional ocean projections for living marine  
690 resource management in a changing climate, *ICES Journal of Marine Science*, 78, 1969–  
691 1987, <https://doi.org/10.1093/icesjms/fsab100>, 2021.
- 692 20. Dunne, J. P., Horowitz, L. W., Adcroft, A. J., Ginoux, P., Held, I. M., John, J. G., Krasting, J.  
693 P., Malyshev, S., Naik, V., Paulot, F., Shevliakova, E., Stock, C. A., Zadeh, N., Balaji, V.,  
694 Blanton, C., Dunne, K. A., Dupuis, C., Durachta, J., Dussin, R., Gauthier, P. P. G., Griffies,  
695 S. M., Guo, H., Hallberg, R. W., Harrison, M., He, J., Hurlin, W., McHugh, C., Menzel, R.,  
696 Milly, P. C. D., Nikonov, S., Paynter, D. J., Ploshay, J., Radhakrishnan, A., Rand, K., Reichl,  
697 B. G., Robinson, T., Schwarzkopf, D. M., Sentman, L. T., Underwood, S., Vahlenkamp,  
698 H., and Winton, M.: The GFDL Earth System Model Version 4.1 (GFDL-ESM 4.1): Overall  
699 coupled model description and simulation characteristic, *Journal of Advances in Modeling*  
700 *Earth Systems*, 12, e2019MS002015. <https://doi.org/10.1029/2019MS002015>, 2020.
- 701 21. Ezer, T.: Detecting changes in the transport of the Gulf Stream and the Atlantic overturning  
702 circulation from coastal sea level data: The extreme decline in 2009–2010 and estimated  
703 variations for 1935–2012, *Global and Planetary Change*, 129, 23–36.  
704 <https://doi.org/10.1016/j.gloplacha.2015.03.002>, 2015.

- 705 22. Ezer, T.: Regional differences in sea level rise between the Mid-Atlantic Bight and the South  
706 Atlantic Bight: Is the Gulf Stream to blame?, *Earth's Future*, 7, 771–783.  
707 <https://doi.org/10.1029/2019EF001174>, 2019.
- 708 23. Ezer, T., and Atkinson, L. P.: Accelerated flooding along the U.S. EastCoast: On the impact  
709 of sea-level rise,tides, storms, the Gulf Stream, and the North Atlantic Oscillations, *Earth's*  
710 *Future*, 2, 362–382,doi:10.1002/2014EF000252, 2014.
- 711 24. Ezer, T., Atkinson, L. P., Corlett, W. B., and Blanco, J. L.: Gulf Stream's induced sea level  
712 rise and variability along the US mid-Atlantic coast, *Journal of Geophysical Research:*  
713 *Oceans*, 118, 685–697, <https://doi.org/10.1002/jgrc.20091>, 2013.
- 714 25. Friedrichs, M. A. M., St-Laurent, P., Xiao, Y., Hofmann, E., Hyde, K., Mannino, A., Najjar,  
715 R. G., Narváez, D. A., Signorini, S.R., Tian, H., Wilkin, J., Yao, Y., Xue, J.: Ocean  
716 circulation causes strong variability in the Mid-Atlantic Bight nitrogen budget. *Journal of*  
717 *Geophysical Research: Oceans*, 124, 113–134. <https://doi.org/10.1029/2018JC014424>, 2019.
- 718 26.
- 719 27. Goddard, P. B., Yin, J., Griffies, S. M., and Zhang, S.: An extreme event of sea-level rise  
720 along the Northeast coast of North America in 2009–2010, *Nature Communications*, 6,  
721 <https://doi.org/10.1038/ncomms7346>, 2015.
- 722 28. Gomez, F.A., Lee, S.K., Hernandez, F.J., Chiaverano, L.M., Muller-Karger, F.E., Liu, Y.,  
723 and Lamkin, J.T.: ENSO-induced co-variability of Salinity, Plankton Biomass and Coastal  
724 Currents in the Northern Gulf of Mexico. *Scientific reports*, 9, 178,  
725 <https://doi.org/10.1038/s41598-018-36655-y>, 2019.
- 726 29. Gomez, F. A., Lee, S.-K., Stock, C. A., Ross, A.C., Resplandy, L., Siedlecki, S.A., Tagklis,  
727 F., and Salisbury, J. E.: RC4USCoast: A river chemistry dataset for regional ocean model

728 applications in the U.S. East, Gulf of Mexico, and West Coasts, Earth System Science Data,  
729 <https://doi.org/10.5194/essd-2022-341>, 2022.

730 30. Gomez, F. A., Ross, A. C., Lee, S.-K., Volkov, D., Kim, D., John, J. G., & Stock, C. A.:  
731 Wind control of the interannual ocean-biogeochemical variability in the South Atlantic Bight,  
732 Journal of Geophysical Research: Oceans, 131, e2025JC023322, 2026.

733 31. Gomez, F.A., Wanninkhof, R., Barbero, L., and Lee, S.-K.: Mississippi River Chemistry  
734 Impacts on the Interannual Variability of Aragonite Saturation State in the Northern Gulf of  
735 Mexico, Journal of Geophysical Research: Oceans, 129 , e2023JC020436, 2024.

736 32. Gomez, F.A., Wanninkhof, R., Barbero, L., Lee, S.K., and Hernandez, F. J.: Seasonal  
737 patterns of surface inorganic carbon system variables in the Gulf of Mexico inferred from a  
738 regional high-resolution ocean biogeochemical model, Biogeosciences, 17, 1685–1700.  
739 <https://doi.org/10.5194/bg-17-1685-2020>, 2020.

740 33. Greatbatch, R. J.: A note on the representation of steric sea level in models that conserve  
741 volume rather than mass. Journal of Geophysical Research: Oceans, 12, 767–12,771, 1994.

742 34. Griffies, S. M., and Greatbatch, R. J.: Physical processes that impact the evolution of global  
743 mean sea level in ocean climate models, Ocean Modelling, 51, 37–72, 2012.

744 35. Griffies, S. M., Yin, J., Durack, P. J., Goddard, P., Bates, S. C., Behrens, E., Bentsen, M., Bi,  
745 D., Biastoch, A., Böning, C., Bozec, A., Chassignet, E., Danabasoglu, G., Danilov, S.,  
746 Domingues, C. M., Drange, H., Farneti, R., Fernandez, E., Greatebatch, R. J., Holland, D.  
747 M., Ilicak, M., Large, W. G., Lorbacher, K., Lu, J., Marsland, S. J., Mishra, A., Nurser, A. J.  
748 G., Salas y Mélia, D., Palter, J. B., Samuels, B. L., Schröter, Schwarzkopf, F. U., Sidorenko,  
749 D., Treguier, A.-M., Tseng, Y. H., Tsujino, H., Uotila, P., Valcke, S., Voldoire, A., Wang,  
750 Q., Winton, M., and Zhang, X.: An assessment of global and regional sea level for years

- 751 1993–2007 in a suite of interannual CORE-II simulations, *Ocean Modelling*, 78, 35-89,  
752 <https://doi.org/10.1016/j.ocemod.2014.03.004>, 2014.
- 753 36. Hameed, S., C. Wolfe, L. P., and Chi, L.: Impact of the Atlantic Meridional Mode on Gulf  
754 Stream North Wall Position, *Journal of Climate*, 31, 8875–8894,  
755 <https://doi.org/10.1175/JCLI-D-18-0098.1>, 2018.
- 756 37. Hermans, T. H. J., Gregory, J. M., Palmer, M. D., Ringer, M. A., Katsman, C. A., and  
757 Slangen, A. B. A.: Projecting global mean sea-level change using CMIP6 models,  
758 *Geophysical Research Letters*, 48, e2020GL092064. <https://doi.org/10.1029/2020GL092064>,  
759 2021.
- 760 38. Hersbach, H., Bell, B., Berrisford, P., Hirahara, S., Horányi, A., Muñoz-Sabater, J., Nicolas,  
761 J., Peubey, C., Radu, R., Schepers, D., Simmons, A., Soci, C., Abdalla, S., Abellan, X.,  
762 Balsamo, G., Bechtold, P., Biavati, G., Bidlot, J., Bonavita, M., De Chiara, G., Dahlgren, P.,  
763 Dee, D., Diamantakis, M., Dragani, R., Flemming, J., Forbes, R., Fuentes, M., Geer, A.,  
764 Haimberger, L., Healy, S., Hogan, R. J., Hólm, E., Janisková, M., Keeley, S., Laloyaux, P.,  
765 Lopez, P., Lupu, C., Radnoti, G., de Rosnay, P., Rozum, I., Vamborg, F., Villaume, S., and  
766 Thépaut, J.-N.: The ERA5 Global Reanalysis, *Quarterly Journal of the Royal Meteorological*  
767 *Society*, 146, 1999–2049, <https://doi.org/10.1002/qj.3803>, 2020.
- 768 39. Huang, L., Volkov, D. L., Dong, S., and Schmid, C.: On the rapid warming in the subtropical  
769 North Atlantic in 2011–2021, *Geophysical Research Letters*, 52, e2025GL116280.  
770 <https://doi.org/10.1029/2025GL116280>, 2025.
- 771 40. Intergovernmental Panel On Climate Change (Ippc). Climate Change 2021 – The Physical  
772 Science Basis: Working Group I Contribution to the Sixth Assessment Report of the

773 Intergovernmental Panel on Climate Change. (Cambridge University Press, 2023).  
774 doi:10.1017/9781009157896.

775 41.

776 42. Jeong, D.I., and Sushama, L.: Projected Changes to Mean and Extreme Surface Wind Speeds  
777 for North America Based on Regional Climate Model Simulations, *Atmosphere*, 10, 497,  
778 <https://doi.org/10.3390/atmos10090497>, 2019.

779 43. Jin, C., Liu, H., Lin, P., Lyu, K., and Li, Y.: Uncertainties in the projection of stereodynamic  
780 sea level in CMIP6 models, *Geophysical Research Letters*, 52, e2024GL113691.  
781 <https://doi.org/10.1029/2024GL113691>, 2025.

782 44. Karnauskas, M., Schirripa, M.J., Craig, K., Cook, G, Kelble, C., Agar, J., Black, B., Enfield,  
783 D., Lindo-Atichati, D., Muhling, B., Purcell, K., Richards, P., and Wang C. Evidence of  
784 climate-driven ecosystem reorganization in the Gulf of Mexico, *Global Change Biology*, 21,  
785 2554–2568, 2015.

786 45. Karnauskas, M., Schirripa, M.J., Kelble, C.K., Cook, G.S., and Craig, J.K.: Ecosystem status  
787 report for the Gulf of Mexico, NOAA Technical Memorandum NMFS-SEFSC-653, 2013

788 46. Koul, V., Ross, A. C., Stock, C., Zhang, L., Delworth, T., and Wittenberg, A.: A predicted  
789 pause in the rapid warming of the Northwest Atlantic Shelf in the coming decade,  
790 *Geophysical Research Letters*, 51, e2024GL110946, <https://doi.org/10.1029/2024GL110946>,  
791 2024.

792 47. Lee, T. N., Yoder, J. A., and Atkinson, L. P.: Gulf Stream frontal eddy influence on  
793 productivity of the 857 southeast US Continental Shelf, *Journal of Geophysical Research:*  
794 *Oceans*, 96, 191–205, <https://doi.org/10.1029/91jc02450>, 1991.

- 795 48. Lellouche, J., Greiner, E., Bourdallé-Badie, R., Garric, G., Melet, A., Dréville, M., Bricaud,  
796 C., Hamon, M., Le Galloudec, O., Regnier, C., Candela, T., Testut, C., Gasparin, F.,  
797 Ruggiero, G., Benkiran, M., Drillet, Y., and Le Traon, P.: The Copernicus Global 1/12  
798 Oceanic and Sea Ice GLORYS12 Reanalysis, *Frontiers in Earth Science*, 9, 698876,  
799 <https://doi.org/10.3389/feart.2021.698876>, 2021.
- 800 49. Levermann, A., Griesel, A., Hofmann, M., Montoya, M., and Rahmstorf, S.: Dynamic sea  
801 level changes following changes in the thermohaline circulation, *Climate Dynamics*, 24,  
802 347–354, <https://doi.org/10.1007/s00382-004-0505-y>, 2005.
- 803 50. Li, D., Chang, P., Yeager, S. G., Danabasoglu, G., Castruccio, F. S., Small, Wang, H.,  
804 Zhang, Q., and Gopal, A.: The impact of horizontal resolution on projected sea-level rise  
805 along US east continental shelf with the community earth system model, *Journal of Advances  
806 in Modeling Earth Systems*, 14, e2021MS002868, 2022.
- 807 51. Lin, S. J.: A “vertically Lagrangian” finite-volume dynamical core for global models,  
808 *Monthly Weather Review*, 132, 2293–2307. 2004.
- 809 52. Little, C. M., Hu, A., Hughes, C. W., McCarthy, G. D., Piecuch, C. G., Ponte, R. M., and  
810 Thomas, M. D.: The Relationship between U.S. East Coast sea level and the Atlantic  
811 Meridional Overturning Circulation: A review, *Journal of Geophysical Research: Oceans*, 124,  
812 6435–6458, <https://doi.org/10.1029/2019JC015152>, 2019.
- 813 53. Little, C. M., Piecuch, C. G., and Ponte, R. M.: On the relationship between the meridional  
814 overturning circulation, alongshore wind stress, and United States East Coast sea level in the  
815 Community Earth System Model Large Ensemble, *Journal of Geophysical Research: Oceans*  
816 122, 4554–4568, <https://doi.org/10.1002/2017JC012713>, 2017.

- 817 54. Liu, Y., Lee, S.-K., Enfield, D. B., Muhling, B. A., Lamkin, J. T., Muller-Karger, F. E., and  
818 Roffer, M. A.: Potential impact of climate change on the Intra-Americas Sea: Part-1. A  
819 dynamic downscaling of the CMIP5 model projections, *Journal of Marine Systems*, 148, 56-  
820 69, <https://doi.org/10.1016/j.jmarsys.2015.01.007>, 2015.
- 821 55. Liu, Y., Lee, S.-K., Muhling, B.A., Lamkin, J.T., and Enfield, D.B.: Significant reduction of  
822 the Loop Current in the 21st century and its impact on the Gulf of Mexico, *Journal of*  
823 *Geophysical Research:Oceans*, 117, C05039. <http://dx.doi.org/10.1029/2011JC007555>, 2012.
- 824 56. McCarthy, G. D., Smeed D.A., Johns W.E., Frajka-Williams E., Moat B.I., Rayner D.,  
825 Baringer M.O., Meinen C.S., Collins, J., and Bryden H.L.: Measuring the Atlantic  
826 Meridional Overturning Circulation at 26°N. *Progress in Oceanography*, 130, 91-111,  
827 <http://dx.doi.org/10.1016/j.pocean.2014.10.006>, 2015.
- 828 57. Meehl, G. A., Senior, C. A., Eyring, V., Flato, G., Lamarque, J.-F., Stouffer, R. J., Taylor, K.  
829 E., and Schlund, M.: Context for interpreting equilibrium climate sensitivity and transient  
830 climate response from the CMIP6 Earth system models. *Science Advances*, 6, eaba1981,  
831 2020.
- 832 58. Meinen, C. S., Johns, W. E., Moat, B. I., Smith, R. H., Johns, E. M., Rayner, D., Frajka-  
833 Williams, E., Garcia, R.F., and Garzoli, S. L.: Structure and variability of the Antilles  
834 Current at 26.5°N, *Journal of Geophysical Research: Oceans*, 124, 3700–3723.  
835 <https://doi.org/10.1029/2018JC014836>, 2019.
- 836 59. Minobe, S., Terada, M., Qiu, B., and Schneider, N.: Western boundary sea level: A theory,  
837 rule of thumb, and application to climate models, *Journal of Physical Oceanography*, 47,  
838 957–977, <https://doi.org/10.1175/JPO-D-16-0144.1>, 2017.

- 839 60. Muller-Karger, F. E., Smith, J. P., Werner, S., Chen, R., Roffer, M., Liu, Y., Muhling, B.,  
840 Lindo-Atichati, D., Lamkin, J., Cerdeira-Estrada, S., and Enfield, D. B.: Natural variability of  
841 surface oceanographic conditions in the offshore Gulf of Mexico, *Progress in Oceanography*,  
842 134, 54–76. 2015.
- 843 61. New, A. L., Smeed, D. A., Czaja A., Blaker A.T., Mecking J. V., Mathews J.P., and  
844 Sanchez-Franks A.: Labrador Slope Water connects the subarctic with the Gulf Stream.  
845 *Environ. Res. Lett.* 16, 084019, <https://doi.org/10.1088/1748-9326/ac1293>, 2021.
- 846 62. O'Neill, B. C., Tebaldi, C., van Vuuren, D. P., Eyring, V., Friedlingstein, P., Hurtt, G.,  
847 Knutti, R., Kriegler, E., Lamarque, J.-F., Lowe, J., Meehl, G. A., Moss, R., Riahi, K., and  
848 Sanderson, B. M.: The Scenario Model Intercomparison Project (ScenarioMIP) for CMIP6,  
849 *Geoscientific Model Development*, 9, 3461–3482, <https://doi.org/10.5194/gmd-9-3461-2016>,  
850 2016.
- 851 63. Park, J., and Sweet, W.: Accelerated sea level rise and Florida Current transport. *Ocean*  
852 *Science*, 11, 607–615. <https://doi.org/10.5194/os-11-607-2015>, 2015.
- 853 64. Pershing A. J., Alexander M. A., Hernandez C. M., Kerr L. A., Le Bris A., Mills K. E., Nye  
854 J. A., Record N. R., Scannell H. A., Scott J. D., Sherwood G. D., and Thomas A. C.: Slow  
855 adaptation in the face of rapid warming leads to collapse of the Gulf of Maine cod fishery,  
856 *Science*, 350, 809–812, 2015.
- 857 65. Pozo Buil M., Jacox, M. G., Fiechter, J., Alexander, M.A., Bograd, S.J., Curchitser, E.N.,  
858 Edwards, C.A., Rykaczewski, R.R., and Stock, C.A.: A Dynamically Downscaled Ensemble  
859 of Future Projections for the California Current System, *Frontiers Marine Sciences*,  
860 8:612874, doi: 10.3389/fmars.2021.612874, 2021.

- 861 66. Roberts, M. J., Jackson L. C., Roberts, C.D., Meccia V., Docquier D., Koenigk T., Ortega P.,  
862 Moreno-Chamarro., E., Bellucci, A., Coward, A., Drijfhout, S., Exarchou, E., Gutjahr, O.,  
863 Hewitt, H., Iovino, D., Lohmann, K., Putrasahan, D., Schiemann, R., Seddon, J. Terray, L.,  
864 Xu, X., Zhang, Q., Chang, P., Yeager, S. G., Castruccio, F. S., Zhang, S., and Wu, L.:  
865 Sensitivity of the Atlantic Meridional Overturning Circulation to model resolution in CMIP6  
866 HighResMIP simulations and implications for future changes. *Journal of Advances in*  
867 *Modeling Earth Systems*, 12, e2019MS002014, <https://doi.org/10.1029/2019MS002014>,  
868 2020.
- 869 67. Ross, A. C., Stock, C. A., Adcroft, A., Curchitser, E., Hallberg, R., Harrison, M. J.,  
870 Hedstrom, K., Zadeh, N., Alexander, M., Chen, W., Drenkard, E. J., du Pontavice, H.,  
871 Dussin, R., Gomez, F., John, J. G., Kang, D., Lavoie, D., Resplandy, L., Roobaert, A., Saba,  
872 V., Shin, S.-I., Siedlecki, S., and Simkins, J.: A high-resolution physical–biogeochemical  
873 model for marine resource applications in the northwest Atlantic (MOM6-COBALT-NWA12  
874 v1.0), *Geoscientific Model Development*, 16, 6943–6985, [https://doi.org/10.5194/gmd-16-](https://doi.org/10.5194/gmd-16-6943-2023)  
875 [6943-2023](https://doi.org/10.5194/gmd-16-6943-2023), 2023.
- 876 68. Ross, A. C., Stock, C. A., Koul, V., Delworth, T. L., Lu, F., Wittenberg, A., and Alexander,  
877 M. A.: Dynamically downscaled seasonal ocean forecasts for North American east coast  
878 ecosystems, *Ocean Science*, 20, 1631–1656, <https://doi.org/10.5194/os-20-1631-2024>, 2024.
- 879 69. Rutherford, K., Fennel, K., Garcia Suarez, L., and John, J. G.: Uncertainty in the evolution of  
880 northwestern North Atlantic circulation leads to diverging biogeochemical projections,  
881 *Biogeosciences*, 21, 301–314, <https://doi.org/10.5194/bg-21-301-2024>, 2024.
- 882 70. Saba, V. S., Griffies, S. M., Anderson, W. G., Winton, M., Alexander, M. A., Delworth, T.  
883 L., Hare J.A., Harrison M. J., Rosati A., Vecchi G. A., and Zhang, R.: Enhanced warming of

884 the Northwest Atlantic Ocean under climate change, *Journal of Geophysical Research:*  
885 *Oceans*, 121, 118-132, 2016.

886 71. Sanchez-Franks, A., and Zhang, J.: Decadal variability and shifts of the Gulf Stream path,  
887 *Journal of Climate*, 28, 9825-9838, 2015.

888 72. Seidov, D., Gilman, C., and Haupt, B. J.: Global Ocean Circulation: A Review of the Current  
889 State of Knowledge, *Atmosphere*, 10, 446, 2019.

890 73. Sentman, L. T., Dunne, J. P., Horowitz, L. W., Naik, V., Paulot, F., Ginoux, P., and Zadeh,  
891 N.: Quantifying equilibrium climate sensitivity to atmospheric chemistry and composition  
892 representations in GFDL-CM4.0 and GFDL-ESM4.1., *Geophysical Research Letters*,  
893 53,e2025GL116545. <https://doi.org/10.1029/2025GL116545>, 2026

894 74. Shevliakova, E., Malyshev, S., Martinez-Cano, I., Milly, P. C. D., Pacala, S. W., Ginoux, P.,  
895 Dunne, K. A., Dunne, J. P., Dupuis, C., Findell, K. L., Ghannam, K., Horowitz, L. W.,  
896 Knutson, T. R., Krasting, J. P., Naik, V., Phillipps, P., Zadeh, N., Yu, Y., Zeng, F., and  
897 Zeng, Y.: The land component LM4.1 of the GFDL Earth System Model ESM4.1: Model  
898 description and characteristics of land surface climate and carbon cycling in the historical  
899 simulation, *Journal of Advances in Modeling Earth Systems*, 16, e2023MS003922.  
900 <https://doi.org/10.1029/2023MS003922>, 2024.

901 75. Shin, S., and Alexander, M. A.: Dynamical Downscaling of Future Hydrographic Changes  
902 over the Northwest Atlantic Ocean, *Journal of Climate*, 33, 2871–2890,  
903 <https://doi.org/10.1175/JCLI-D-19-0483.1>, 2020.

904 76. Steinberg, J. M., Griffies, S. M., Krasting, J. P., Piecuch, C. G., and Ross, A. C.: A Link  
905 between U.S. East coast sea level and North Atlantic subtropical ocean heat content, *Journal*

906 of Geophysical Research:Oceans, 129, e2024JC021425.  
907 <https://doi.org/10.1029/2024JC021425>, 2024.

908 77. Stock, C. A., Dunne, J. P., Fan, S., Ginoux, P., John, J., Krasting, J. P., Laufkötter, C.,  
909 Paulot, F., and Zadeh, N.: Ocean Biogeochemistry in GFDL's Earth System Model 4.1 and  
910 Its Response to Increasing Atmospheric CO<sub>2</sub>, *J. Adv. Model. Earth Sy.*, 12,  
911 e2019MS002043, <https://doi.org/10.1029/2019MS002043>, 2020.

912 78. Stock, C. A., Dunne, J. P., Luo, J. Y., Ross, A. C., Van Oostende, N., Zadeh, N., Cordero, T.  
913 J., Liu, X., Teng Y-C.: Photoacclimation and photoadaptation sensitivity in a global ocean  
914 ecosystem model, *Journal of Advances in Modeling Earth Systems*, 17, e2024MS004701.  
915 <https://doi.org/10.1029/2024MS004701>, 2025.

916 79. Tanaka, K. R., Torre, M. P., Saba, V. S., Stock, C. A., and Chen, Y.: An ensemble high-  
917 resolution projection of changes in the future habitat of American lobster and sea scallop in  
918 the Northeast US continental shelf, *Diversity and Distributions*, 26, 987–1001,  
919 <https://doi.org/10.1111/ddi.13069>, 2020.

920 80. Volkov, D. L., Lee, S.-K., Domingues, R., Zhang, H., and Goes, M.: Interannual sea level  
921 variability along the southeastern seaboard of the United States in relation to whom it may  
922 concern: The gyre-scale heat divergence in the North Atlantic, *Geophysical Research Letters*,  
923 46, 7481–7490. <https://doi.org/10.1029/2019GL083596>, 2019.

924 81. Volkov, D.L., Smith, R.H., Garcia, R.F., Smeed, D. A., Moat, B. I, Johns, W. E., and  
925 Baringer, M. O.: Florida Current transport observations reveal four decades of steady state,  
926 *Nature Communications*, 15, 7780, <https://doi.org/10.1038/s41467-024-51879-5>, 2024.

927 82. Volkov, D.L., Zhang, K., Johns, W.E. Willis, J. K., Hobbs, W., Goes, M., Zhang, H., and  
928 Menemenlis, D.: Atlantic meridional overturning circulation increases flood risk along the

- 929 United States southeast coast, *Nature Communications*, 14, 5095,  
930 <https://doi.org/10.1038/s41467-023-40848-z>, 2023.
- 931 83. Wang, Z., Boyer, T., Reagan, J., and Hogan, P.: Upper-Oceanic Warming in the Gulf of  
932 Mexico between 1950 and 2020, *Journal of Climate*, 36, 2721–2734,  
933 <https://doi.org/10.1175/JCLI-D-22-0409.1>, 2023.
- 934 84. Wang, Z. A., Wanninkhof, R., Cai, W.-J., Byrne, R. H., Hu, X., Peng, T.-H., and Huang, W.-  
935 J.: The marine inorganic carbon system along the Gulf of Mexico and Atlantic coasts of the  
936 United States: Insights from a transregional coastal carbon study, *Limnology and*  
937 *Oceanography*, 58, 325–342, 2013.
- 938 85. Wanninkhof, R., Barbero, L., Byrne, R., Cai, W.-J., Zhang, H. Z., Baringer, M., and  
939 Langdon, C.: Ocean acidification along the Gulf Coast and East Coast of the USA,  
940 *Continental Shelf Research*, 98, 54–71. 2015.
- 941 86. Weijer, W., Cheng, W., Garuba, O. A., Hu, A., and Nadiga, B. T.: CMIP6 models predict  
942 significant 21st century decline of the Atlantic Meridional Overturning Circulation,  
943 *Geophysical Research Letters*, 47, e2019GL086075. <https://doi.org/10.1029/2019GL086075>,  
944 2020.
- 945 87. Weinberg, J. R.: Bathymetric shift in the distribution of Atlantic surfclams: response to  
946 warmer ocean temperature, *ICES Journal of Marine Science*, 62, 1444–1453,  
947 <https://doi.org/10.1016/j.icesjms.2005.04.020>, 2005.
- 948 88. Worthington, L. V.: On the north Atlantic circulation, *John Hopkins Oceanographic Studies*,  
949 6, 110, 1976.

- 950 89. Yang, J., and Chen, K.: Profound changes in the seasonal cycle of sea level along the United  
951 States Mid-Atlantic Coast. *Geophysical Research Letters*, 52, e2024GL112273.  
952 <https://doi.org/10.1029/2024GL112273>, 2025.
- 953 90. Yin, J., Schlesinger, M. and Stouffer, R.: Model projections of rapid sea-level rise on the  
954 northeast coast of the United States. *Nature Geosciences*, 2, 262–266,  
955 <https://doi.org/10.1038/ngeo462>, 2009.
- 956 91. Yuan, Y., Castelao, R.M. and He, R.: Variability in along-shelf and cross-shelf circulation in  
957 the South Atlantic Bight, *Continental Shelf Research*, 134, 52-62,  
958 <https://doi.org/10.1016/j.csr.2017.01.006>, 2017.
- 959 92. Zantopp, R., Fischer, J., Visbeck, M., and Karstensen, J.: From interannual to decadal: 17  
960 years of boundary current transports at the exit of the Labrador Sea, *Journal of Geophysical*  
961 *Research: Oceans*, 122, 1724–1748, doi:10.1002/2016JC012271, 2017.
- 962 93. Zhang, W., Alatalo, P., Crockford, T., Hirzel, A.J., Meyer, M.G., Oliver, H., Peacock, E.,  
963 Petitpas, C.M., Sandwith, Z., Smith, W.O., Sosik, H.M., Stanley, R.H.R., Stevens, B.L.F.,  
964 Turner, J.T., and McGillicuddy, D.J.: Cross-shelf exchange associated with a shelf-water  
965 streamer at the Mid-Atlantic Bight shelf edge. *Progress in Oceanography*, 210, 102931, 2023.
- 966 94. Zhao, M., Golaz, J.-C., Held, I. M., Guo, H., Balaji, V., Benson, R., Chen, J. H., Chen, X.,  
967 Donner, L. J., Dunne, J., Dunne, K. A., Durachta, J., Fan, S.-M., Freidenreich, S. M., Garner,  
968 S. T., Ginoux, P., Harris, L., Horowitz, L. W., Krasting, J. P., Langenhorst, A. R., Zhi, L.,  
969 Lin, P., Lin, S. J., Malyshev, S., Mason, E., Milly, P. C. D., Ming, Y., Naik, V., Paulot, F.,  
970 Paynter, D., Phillipps, P. J., Radhakrishnan, A., Ramaswamy, V., Robinson, T.,  
971 Schwarzkopf, D., Seman, C. J., Shevliakova, E., Shen, Z., Shin, H. H., Silvers, L. G., Wilson,  
972 J. R., Winton, M., Wittenberg, A. T., Wyman, B., and Xiang, B.: The GFDL Global

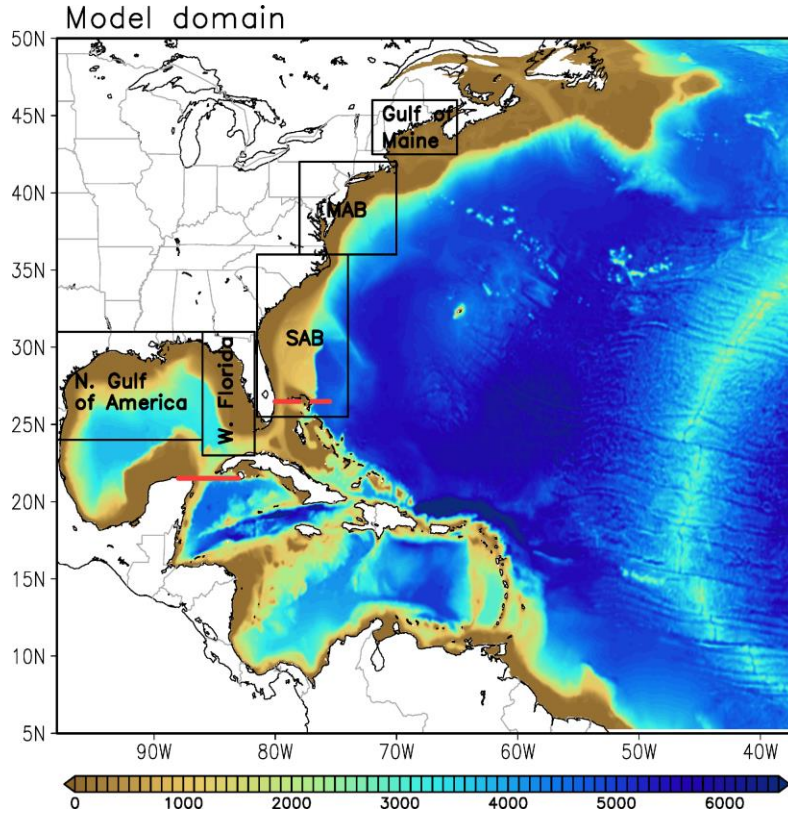
973 Atmosphere and Land Model AM4.0/LM4.0: 1. Simulation characteristics with prescribed  
974 SSTs, *Journal of Advances in Modeling Earth Systems*, 10, 691–734,  
975 <https://doi.org/10.1002/2017ms001208>, 2018.

976 95. Zhao, M., Golaz, J. C., Held, I. M., Guo, H., Balaji, V., Benson, R., Chen, J. H., Chen, X.,  
977 Donner, L. J., Dunne, J. P., Dunne, K., Durachta, J., Fan, S. M., Freidenreich, S. M., Garner,  
978 S. T., Ginoux, P., Harris, L. M., Horowitz, L. W., Krasting, J. P., Langenhorst, A. R., Liang,  
979 Z., Lin, P., Lin, S. J., Malyshev, S. L., Mason, E., Milly, P. C. D., Ming, Y., Naik, V., Paulot,  
980 F., Paynter, D., Phillipps, P., Radhakrishnan, A., Ramaswamy, V., Robinson, T.,  
981 Schwarzkopf, D., Seman, C. J., Shevliakova, E., Shen, Z., Shin, H., Silvers, L. G., Wilson, J.  
982 R., Winton, M., Wittenberg, A. T., Wyman, B., and Xiang, B.: The GFDL Global  
983 Atmosphere and Land Model AM4.0/LM4.0: 2. Model Description, Sensitivity Studies, and  
984 Tuning Strategies, *Journal of Advances in Modeling Earth Systems*, 10, 735–769,  
985 <https://doi.org/10.1002/2017MS001209>, 2018.

986

987 Figure list

988



989

990 **Fig. 1.** MOM6-NWA12 model domain and bathymetry (m). The black boxes indicate the  
991 location of the Northern Gulf of America, West Florida, South Atlantic Bight (SAB), and middle  
992 Atlantic Bight (MAB), and Gulf of Maine for exploring sea-level rise. The red solid lines are the  
993 locations of four major Northwestern Atlantic boundary current systems (Yucatan Current,  
994 Florida Current, Antilles Current (0~500 m), and Deep Western Boundary Current (1,000-  
995 4,000m).

996

997

998

999

1000

1001

1002

1003

1004

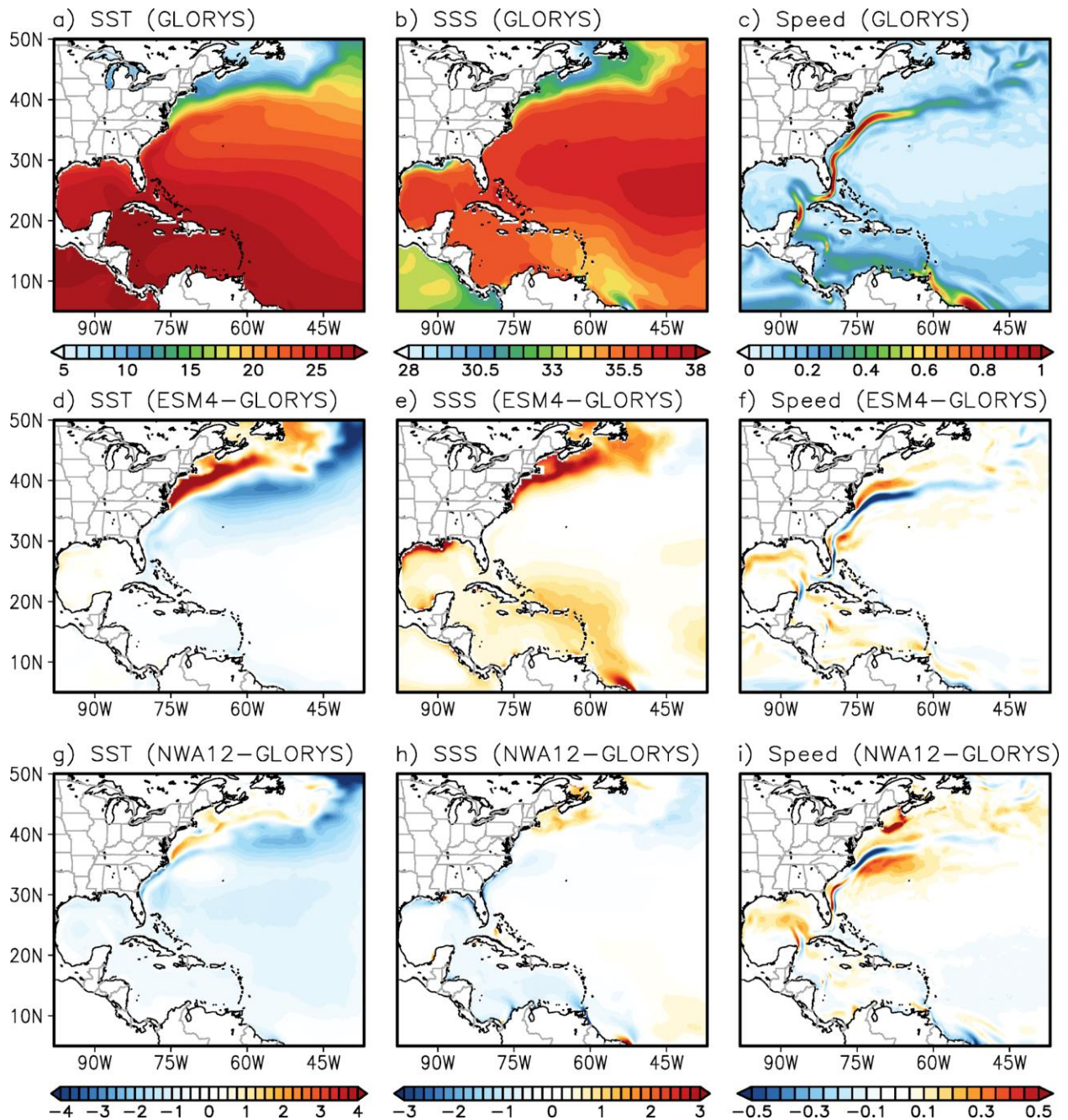
1005

1006

1007

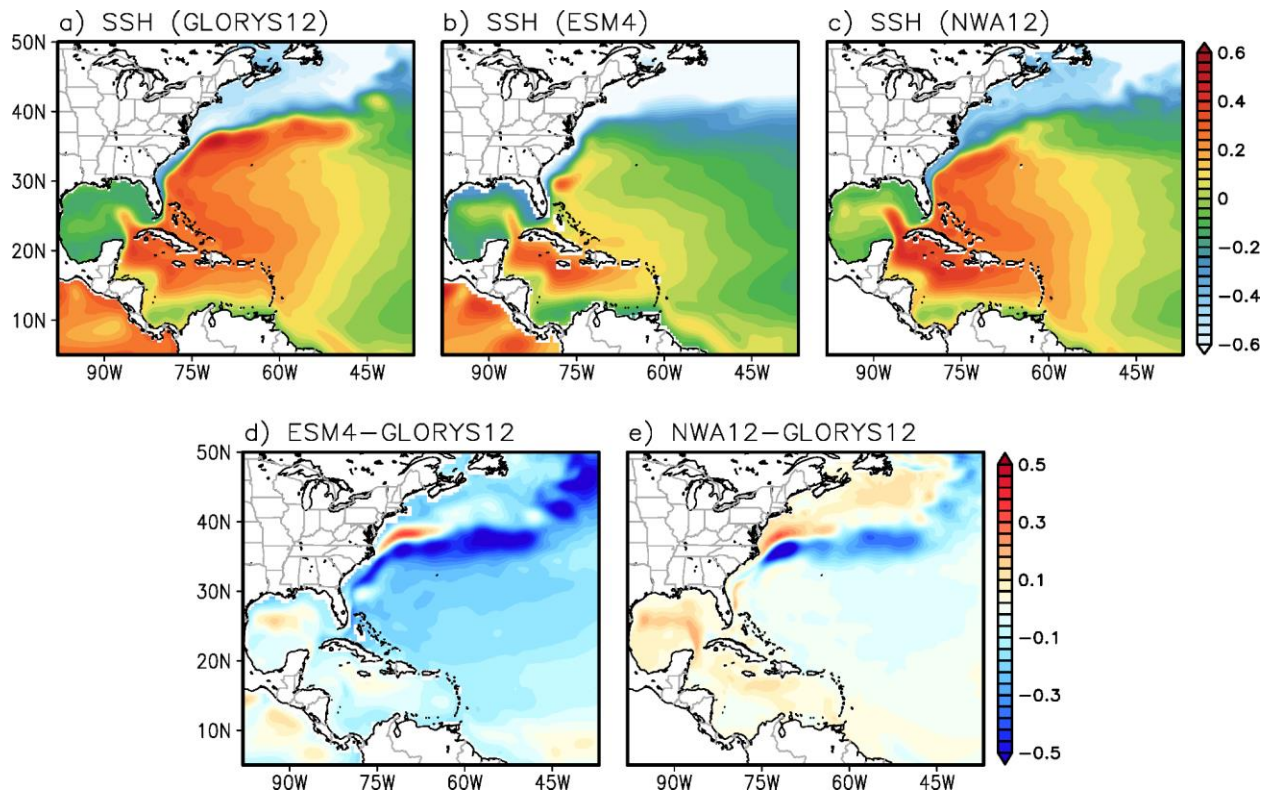
1008

1009



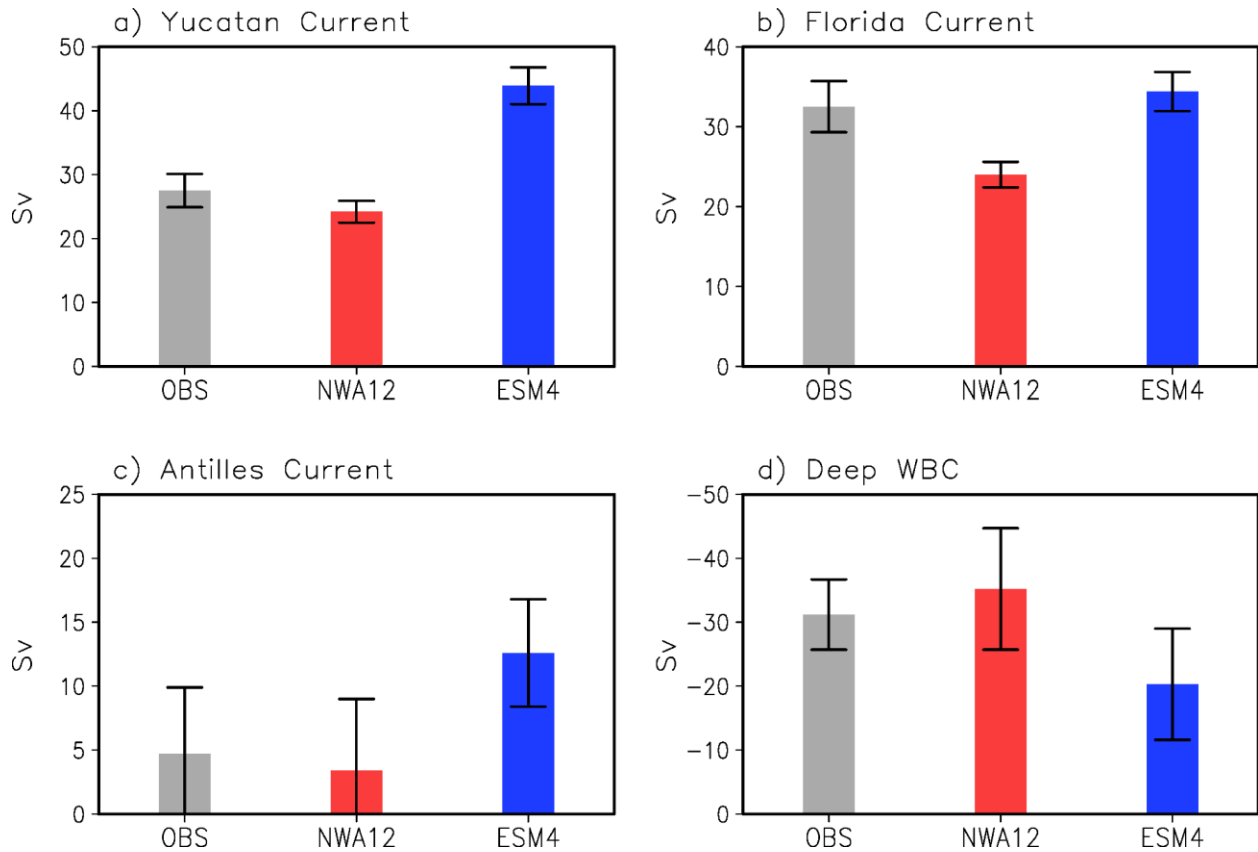
1010  
 1011  
 1012  
 1013  
 1014  
 1015  
 1016  
 1017  
 1018  
 1019

**Fig. 2.** Spatial patterns of the historical (1993–2020) mean (a) sea surface temperature (SST, °C), (b) sea surface salinity (SSS, psu), and (c) surface current speed ( $\text{m s}^{-1}$ ) in GLORYS12. (d)–(f) show the GFDL-ESM4 biases for SST, SSS, and surface current speed. (g)–(i) are the same as (d)–(f), but for MOM6-NWA12.



1020  
 1021  
 1022  
 1023  
 1024  
 1025  
 1026  
 1027

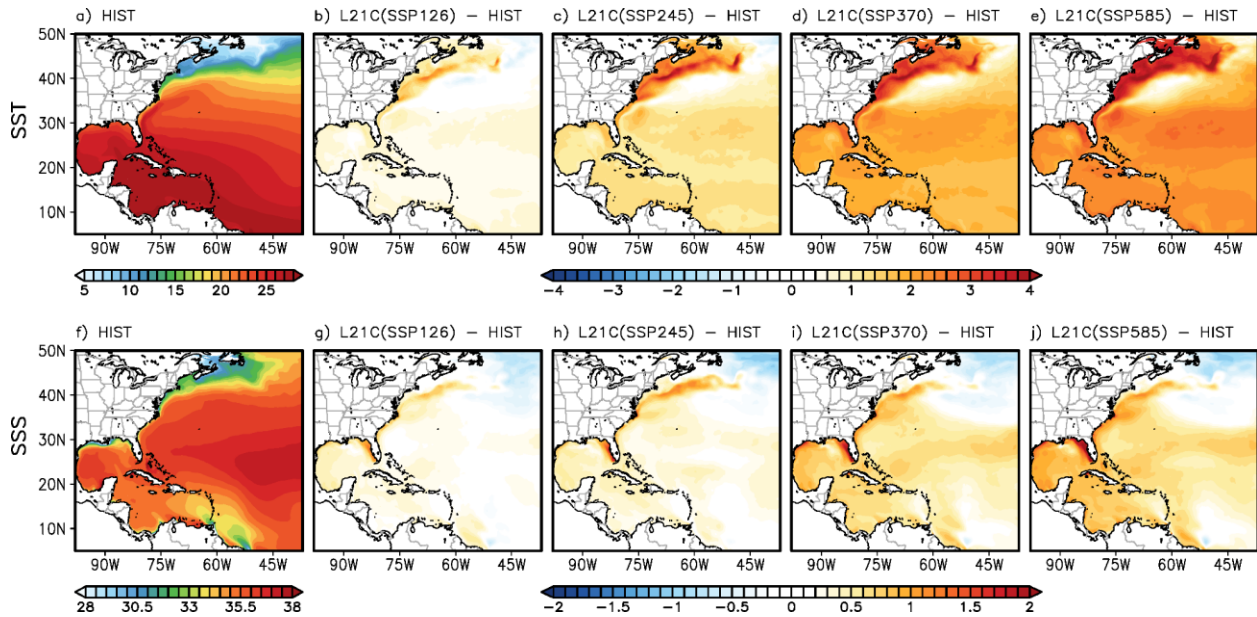
**Fig. 3.** Spatial pattern of the historical (1993-2020) mean sea surface height (SSH, m) in (a) GLORYS12, (b) GFDL-ESM4.1 and (c) MOM6-NWA12. (d) The difference between GFDL-ESM4.1 and GLORYS12. (e) difference between MOM6-NWA12 and GLORYS12.



1028  
1029

1030 **Fig. 4.** The historical mean (1993-2020) of (a) the Yucatan Channel, (b) Florida Current, (c)  
1031 Antilles Current, and (d) Deep Western Boundary Current transport derived from observational  
1032 records (gray bars), MOM6-NWA12 (red bars) and GFDL-ESM4 (blue bars). Note that the  
1033 observational transport records of the Florida Current, Yucatan Current, Antilles Current, and  
1034 Deep Western Boundary Current (DWBC) are from Volkov et al. (2024), Athié et al. (2020),  
1035 Meinen et al. (2019) and Zantopp et al. (2017), respectively.

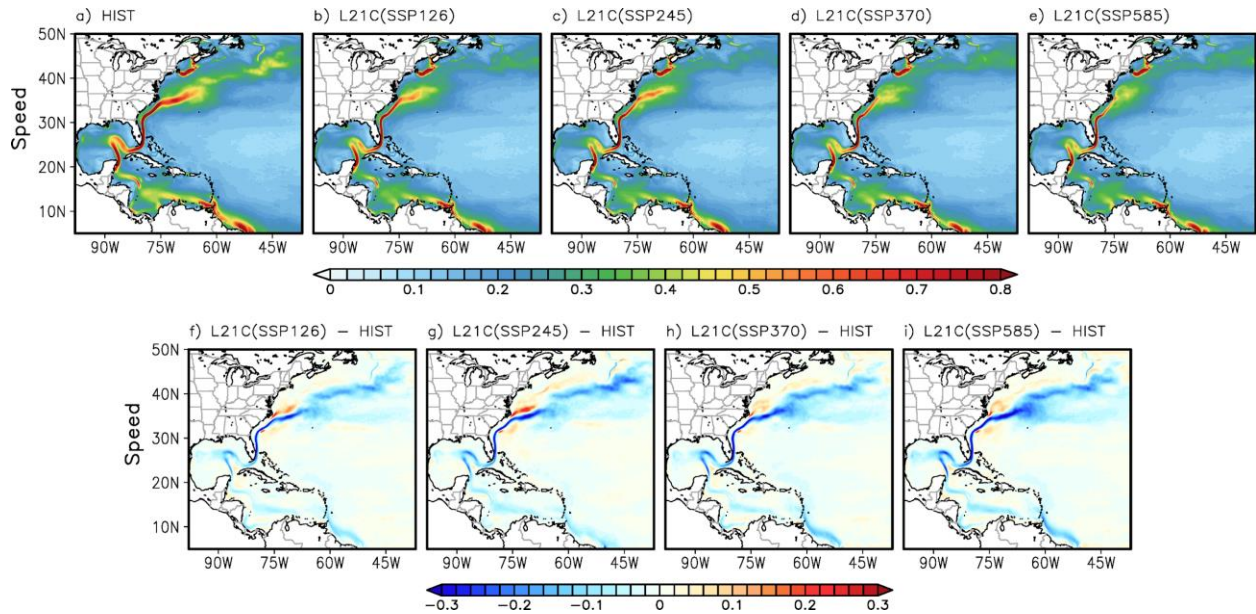
1036  
1037  
1038  
1039  
1040  
1041  
1042  
1043  
1044  
1045  
1046  
1047



1048  
 1049 **Fig. 5.** (a) Spatial patterns of sea surface temperature (SST, °C) derived from MOM6-NWA12  
 1050 during (a) historical period (1993-2020). The differences in SST between the future (2073-2100)  
 1051 and historical periods in the (b) SSP-126, (c) SSP-245, (d) SSP-370 and (e) SSP-585 simulations.  
 1052 (f)-(j) are the same (a)-(e) but for sea surface salinity (SSS, psu).

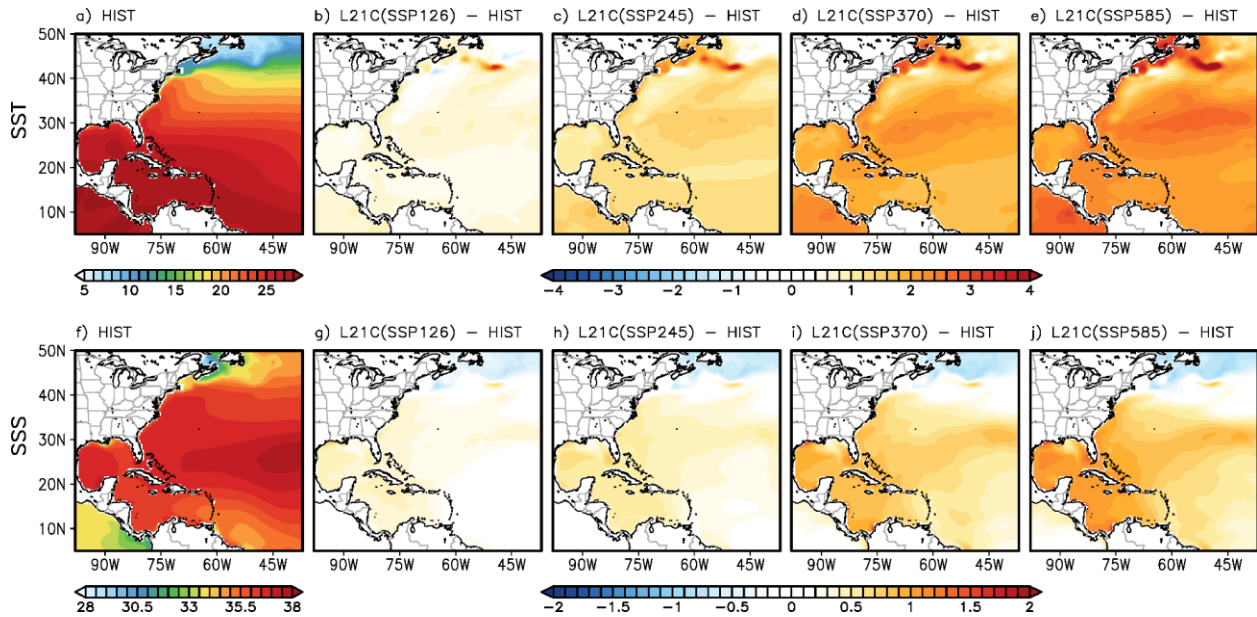
1053  
 1054  
 1055  
 1056  
 1057

1058  
1059  
1060  
1061  
1062  
1063  
1064



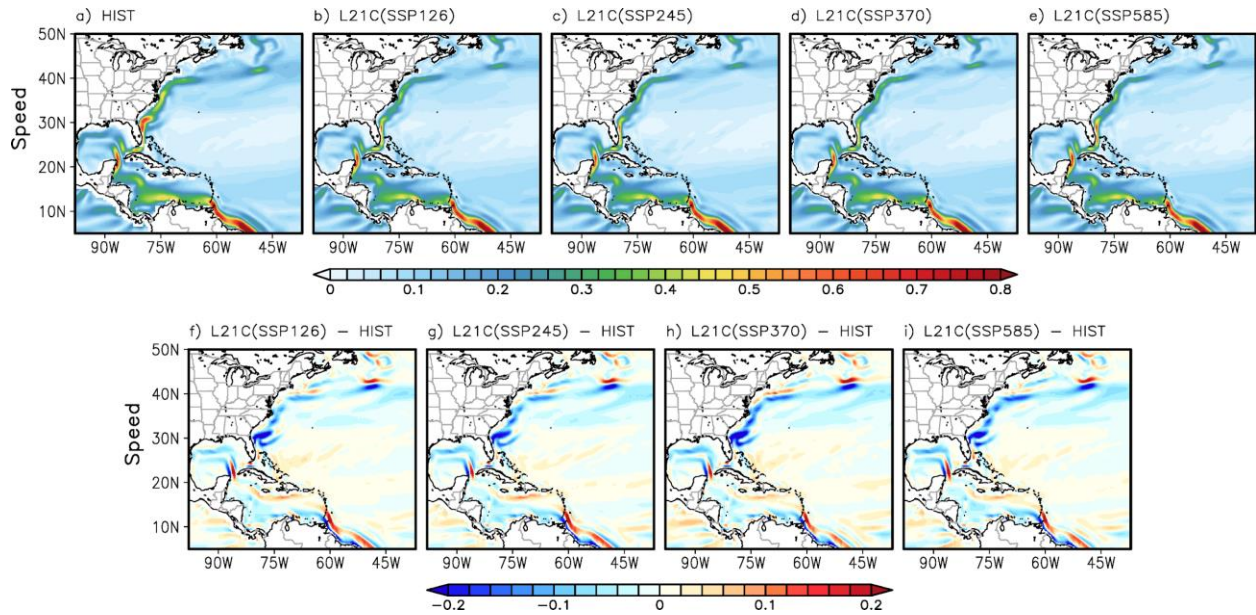
1065  
1066  
1067  
1068  
1069  
1070  
1071  
1072  
1073  
1074

**Fig. 6.** Spatial surface current speed ( $\text{m s}^{-1}$ ) patterns derived from MOM6-NWA12 during (a) the historical (1993-2020) period and future (2073-2100) period in (b) SSP-126, (c) SSP-245, (d) SSP-370 and (e) SSP585 simulations. The difference in surface current speed between the future and historical periods in (f) SSP-126, (g) SSP-245, (h) SSP-370 and (i) SSP585 simulations, respectively.



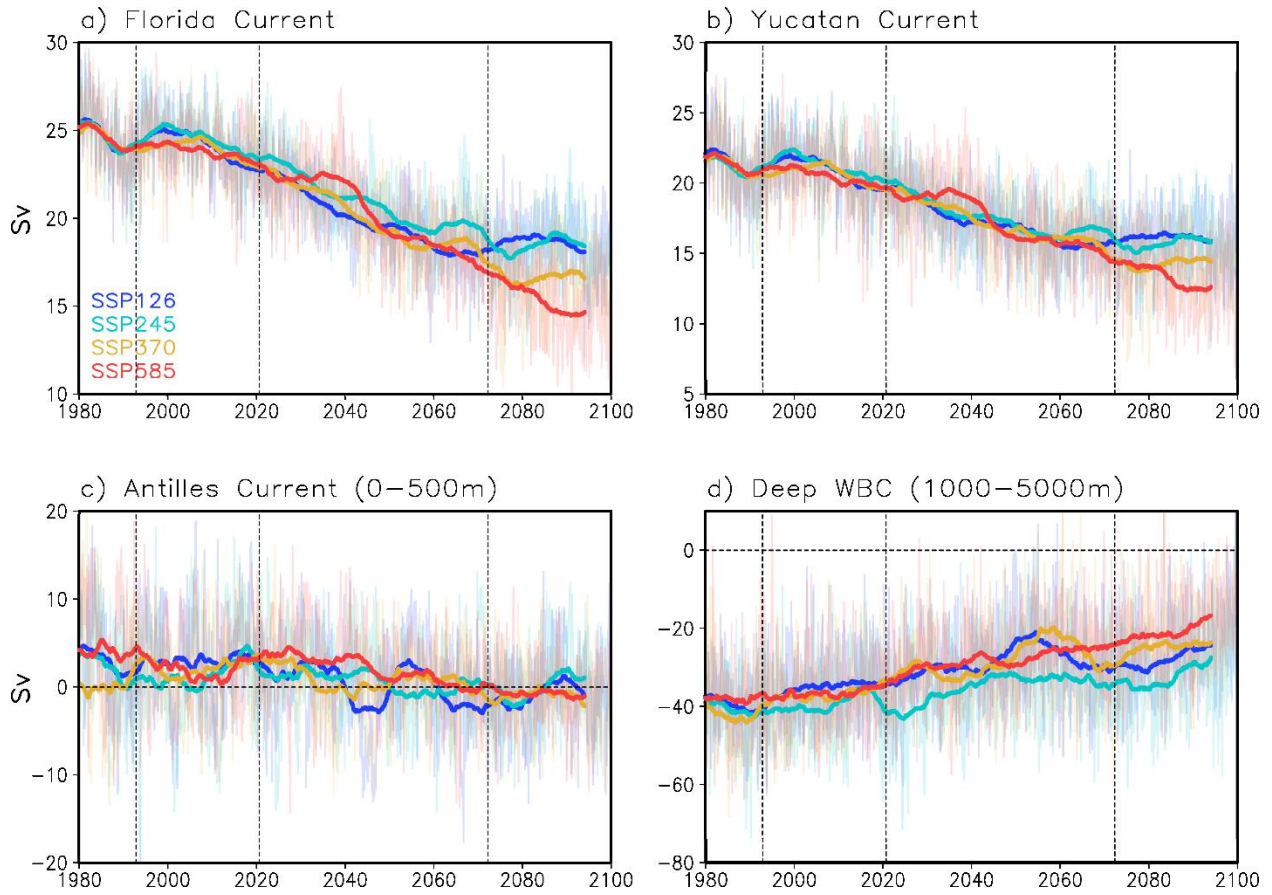
1075  
 1076 **Fig. 7.** (a) Spatial patterns of sea surface temperature (SST) derived from GFDL-ESM4.1 during  
 1077 the historical period (1993-2020). (b)-(e) are the differences in SST between the future (2073-  
 1078 2100) and historical (1993-2020) periods in the SSP-126, SSP-245, SSP-370, and SSP-585  
 1079 simulations, respectively. (f) and (j) are the same (a) and (e) but for the sea surface salinity  
 1080 (SSS).

1081  
 1082



1083  
 1084  
 1085  
 1086  
 1087  
 1088  
 1089  
 1090  
 1091

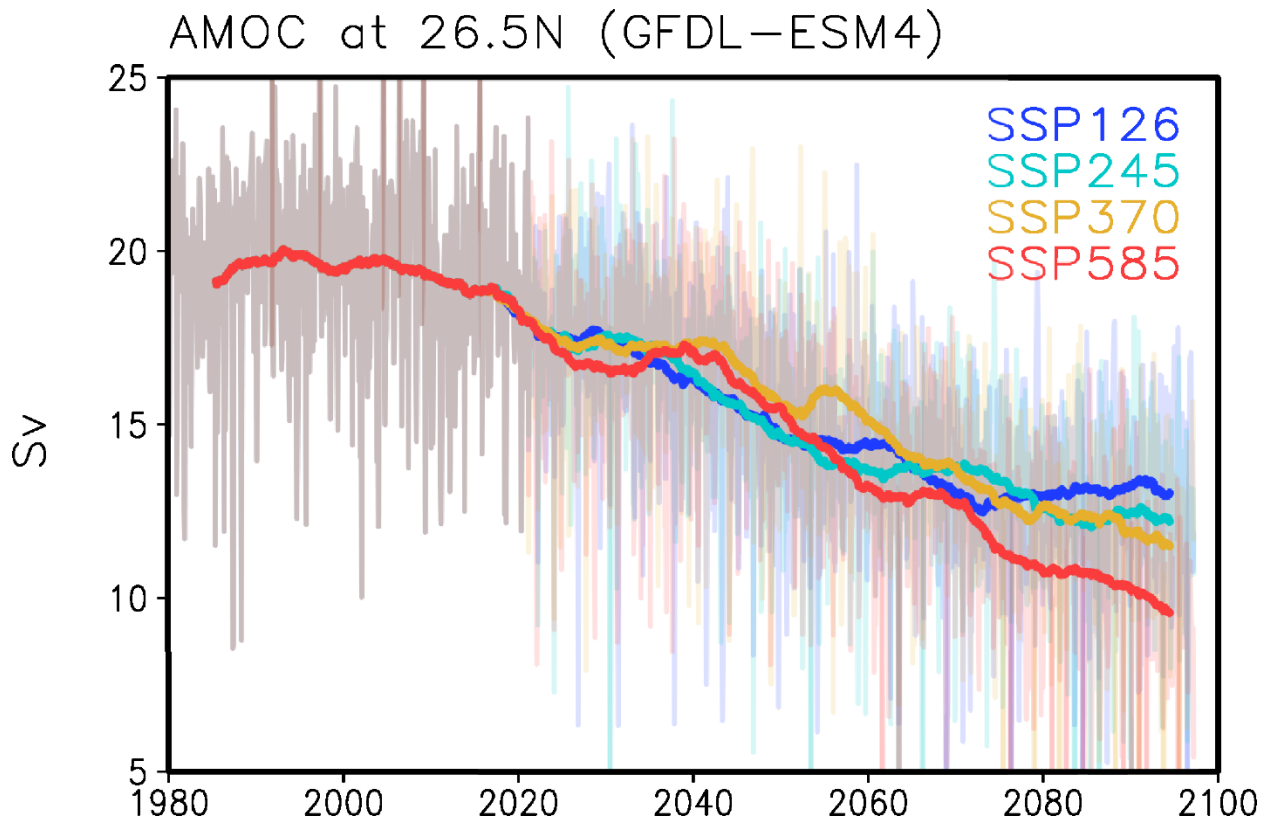
**Fig. 8.** Spatial surface current speed patterns derived from GFDL-ESM4.1 during (a) the historical (1993-2020) period, and future (2073-2100) period in the (b) SSP-126, (c) SSP-245, (d) SSP-370, and (e) SSP-585 simulations. The difference in surface current speed between the future and historical periods in (f) SSP-126, (g) SSP-245, (h) SSP-370, and (i) SSP-585 simulations, respectively.



1092  
 1093  
 1094  
 1095  
 1096  
 1097  
 1098  
 1099  
 1100  
 1101  
 1102  
 1103  
 1104  
 1105  
 1106  
 1107  
 1108  
 1109  
 1110  
 1111  
 1112  
 1113

**Fig. 9.** Time series of (a) the Florida Current transport, (b) transport across the Yucatan Channel, (c) Antilles Current transport and (d) Deep Western Boundary Current transport in MOM6-NWA12. The cyan, green, orange, and red lines are the SSP-126, SSP-245, SSP-370 and SSP-585 simulations, respectively. The bold lines indicate 11-year running means. The dotted lines indicate the historical and future periods. The vertical dotted lines indicate the historical and future averaging periods.

1114



1115

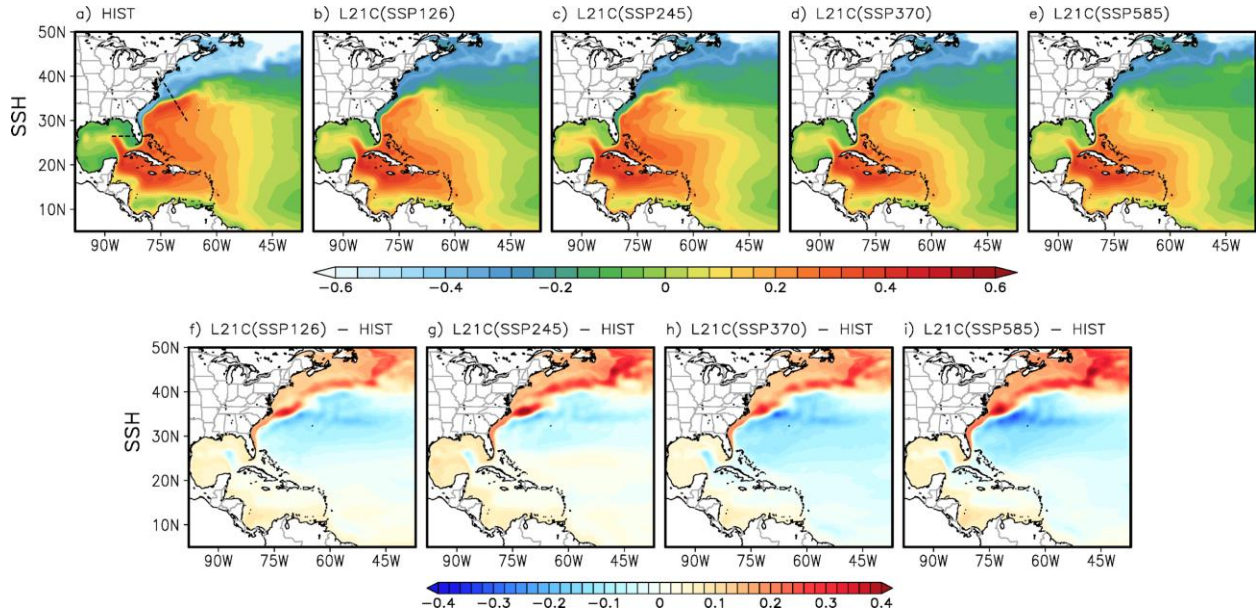
1116

1117

1118

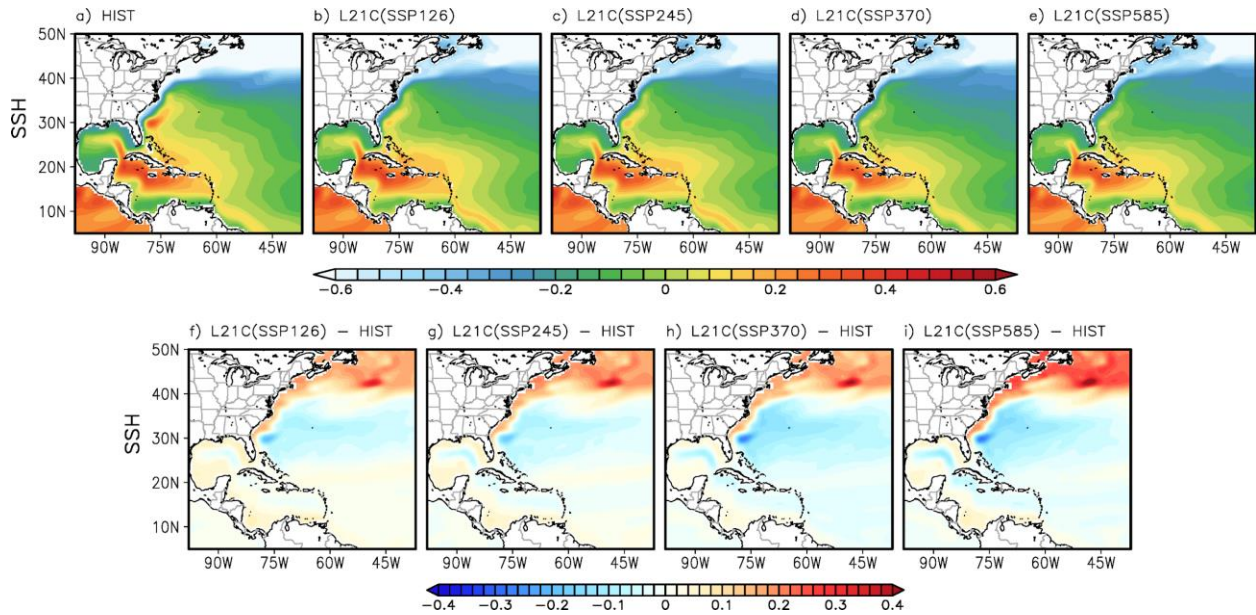
**Fig. 10.** Time series of AMOC in GFDL-ESM4.1. The blue, green, orange, and red lines are the SSP-126, SSP-245, SSP-370 and SSP-585 simulations, respectively.

1119  
1120



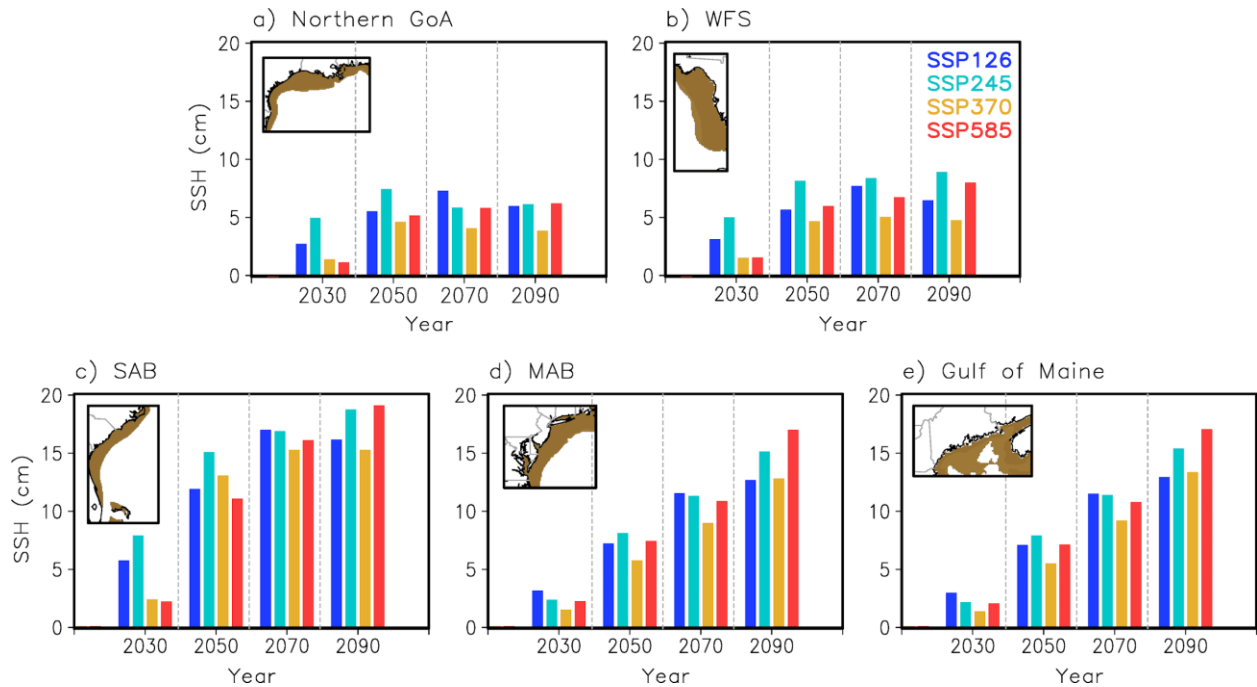
1121  
1122  
1123  
1124  
1125  
1126  
1127  
1128  
1129  
1130  
1131  
1132

**Fig. 11.** Spatial sea surface height (SSH, m) patterns derived from MOM6-NWA12 during (a) the historical (1993-2020) period, and future (2073-2100) period from (b) SSP-126, (c) SSP-245, (d) SSP-370 and (e) SSP-585 simulations. The difference in SSH between the future and historical periods from (f) SSP-126, (g) SSP-245, (h) SSP-370, and (i) SSP-585 simulations, respectively. The black dotted lines in (a) indicate the locations of vertical cross-section used in Fig.15-18.



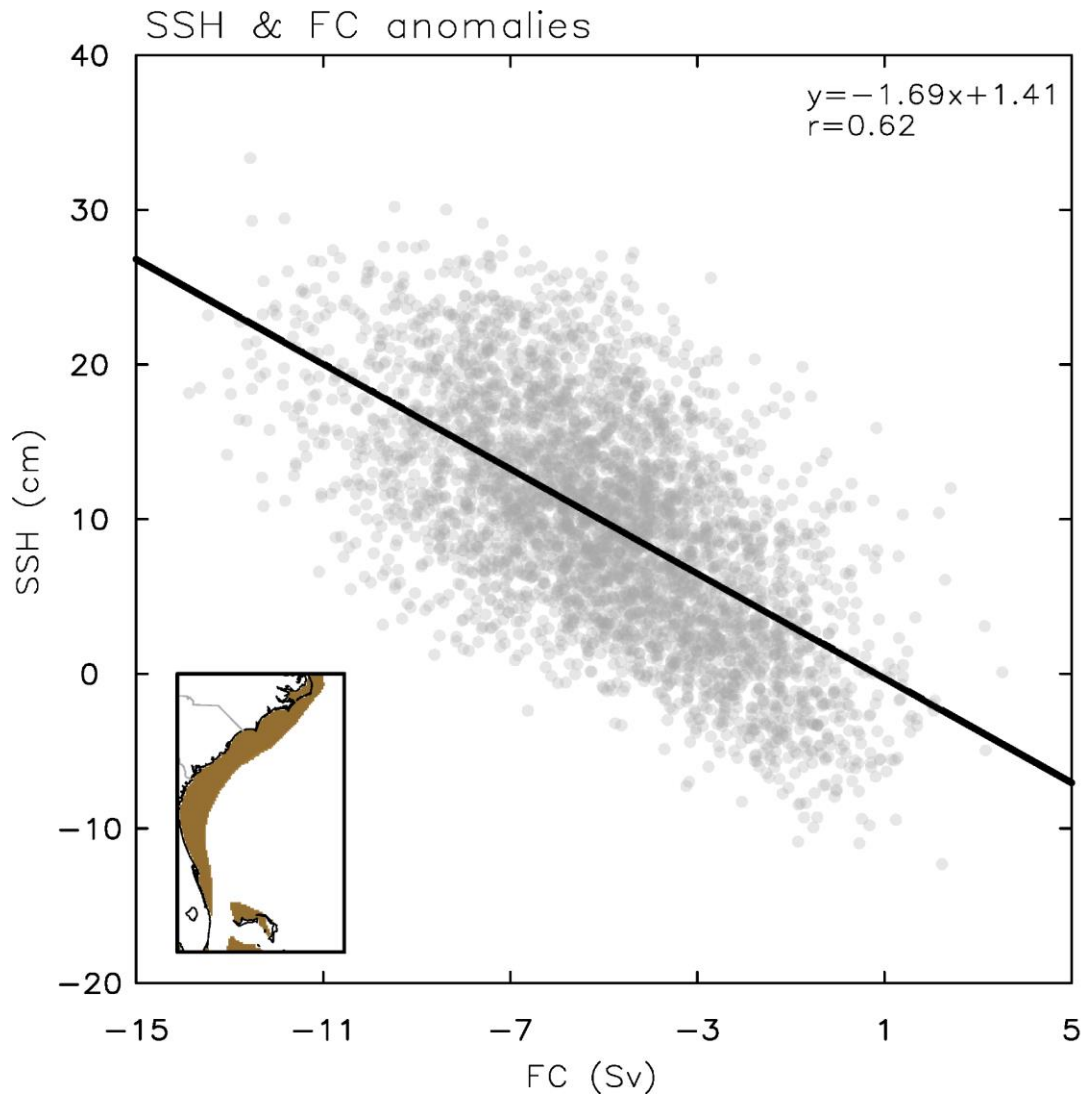
1133  
 1134 **Fig. 12.** Spatial SSH patterns derived from GFDL-ESM4.1 during (a) the historical (1993-2020)  
 1135 period, and future (2073-2100) period from (b) SSP-126, (c) SSP-245, (d) SSP-370, and (e) SSP-  
 1136 585 simulations, respectively. The difference in SSH between the future and historical periods  
 1137 from (f) SSP-126, (g) SSP-245, (h) SSP-370 and (i) SSP-585 simulations, respectively.

1138  
 1139  
 1140  
 1141  
 1142  
 1143  
 1144  
 1145  
 1146  
 1147  
 1148  
 1149  
 1150  
 1151  
 1152  
 1153  
 1154  
 1155



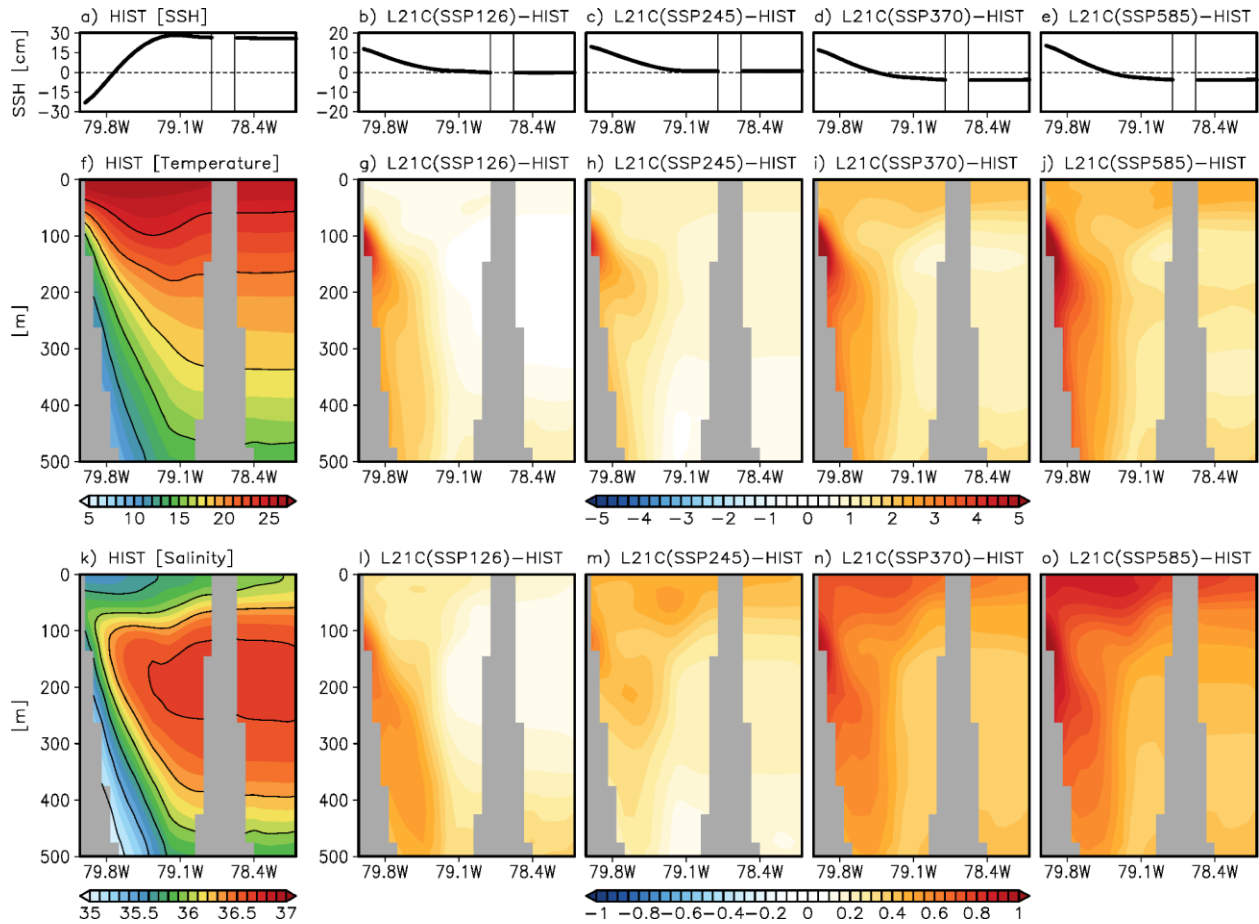
1156  
 1157 **Fig. 13.** Spatially averaged sea level changes (cm) from historical period (1993-2020) in (a) the  
 1158 northern Gulf of America, (b) West Florida shelf, (c) the South Atlantic Bight, (d) the Middle  
 1159 Atlantic Bight, and (e) the Gulf of Maine under the SSP-126 (blue bars), SSP-245 (green bars),  
 1160 SSP-370 (orange bars) and SSP-585 (red bars) simulations. The dynamic sea level changes are  
 1161 spatially averaged over the shelf regions below 200 m depth (brown-colored area in the maps).  
 1162 The years on the x-axis represent the center of a 20-year averaging period (e.g., the value for  
 1163 2030 represents the average from 2021 to 2040).

1164  
 1165  
 1166  
 1167  
 1168  
 1169  
 1170  
 1171  
 1172  
 1173  
 1174  
 1175  
 1176



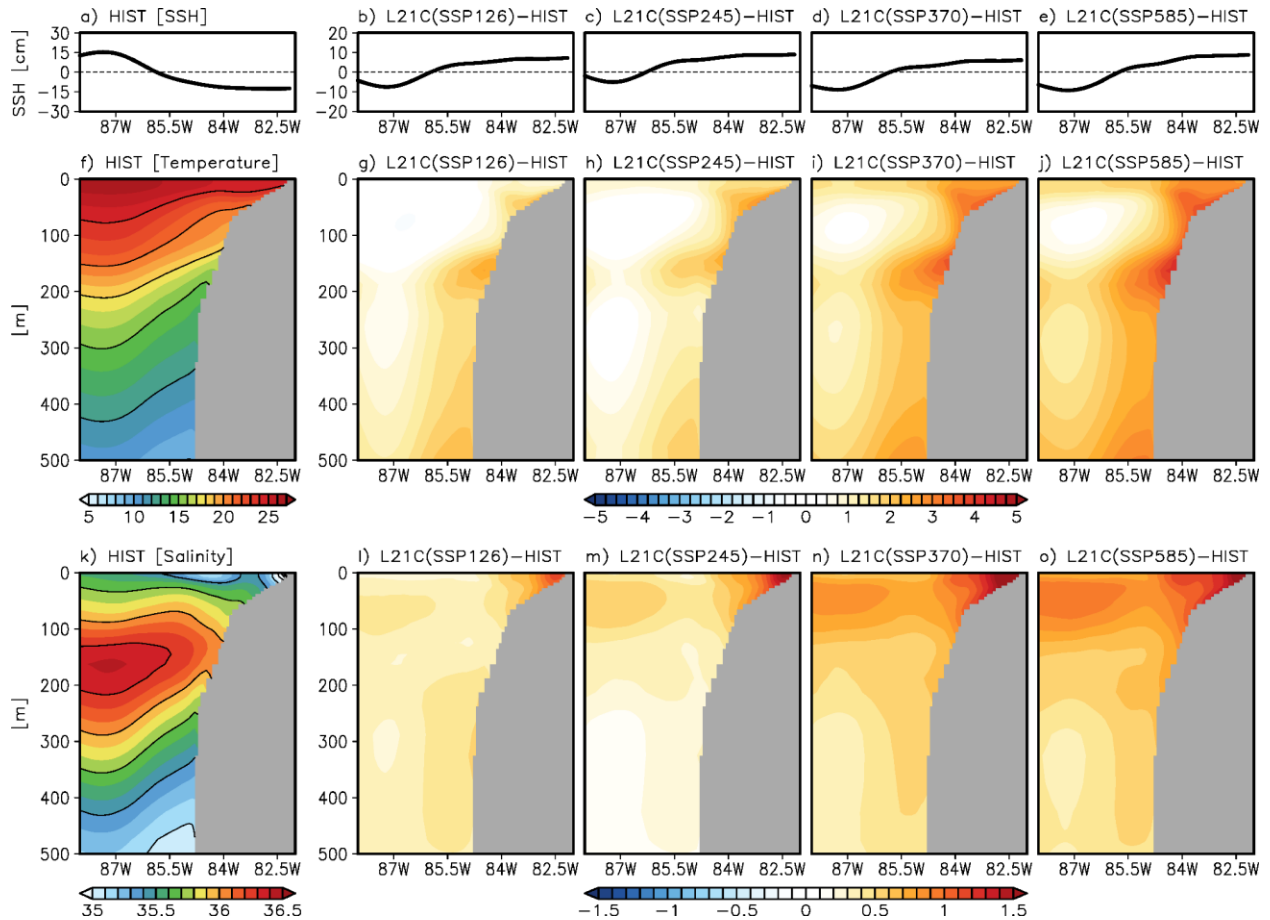
1177  
 1178  
 1179  
 1180  
 1181  
 1182  
 1183  
 1184

**Fig. 14.** Scatter plot of anomalous Florida Current (FC) transport (Sv) versus dynamic sea level (cm) change along the South Atlantic Bight derived from all four SSP simulations. The dynamic sea level change is spatially averaged over the shelf regions below 200 m (brown-colored area in the map).



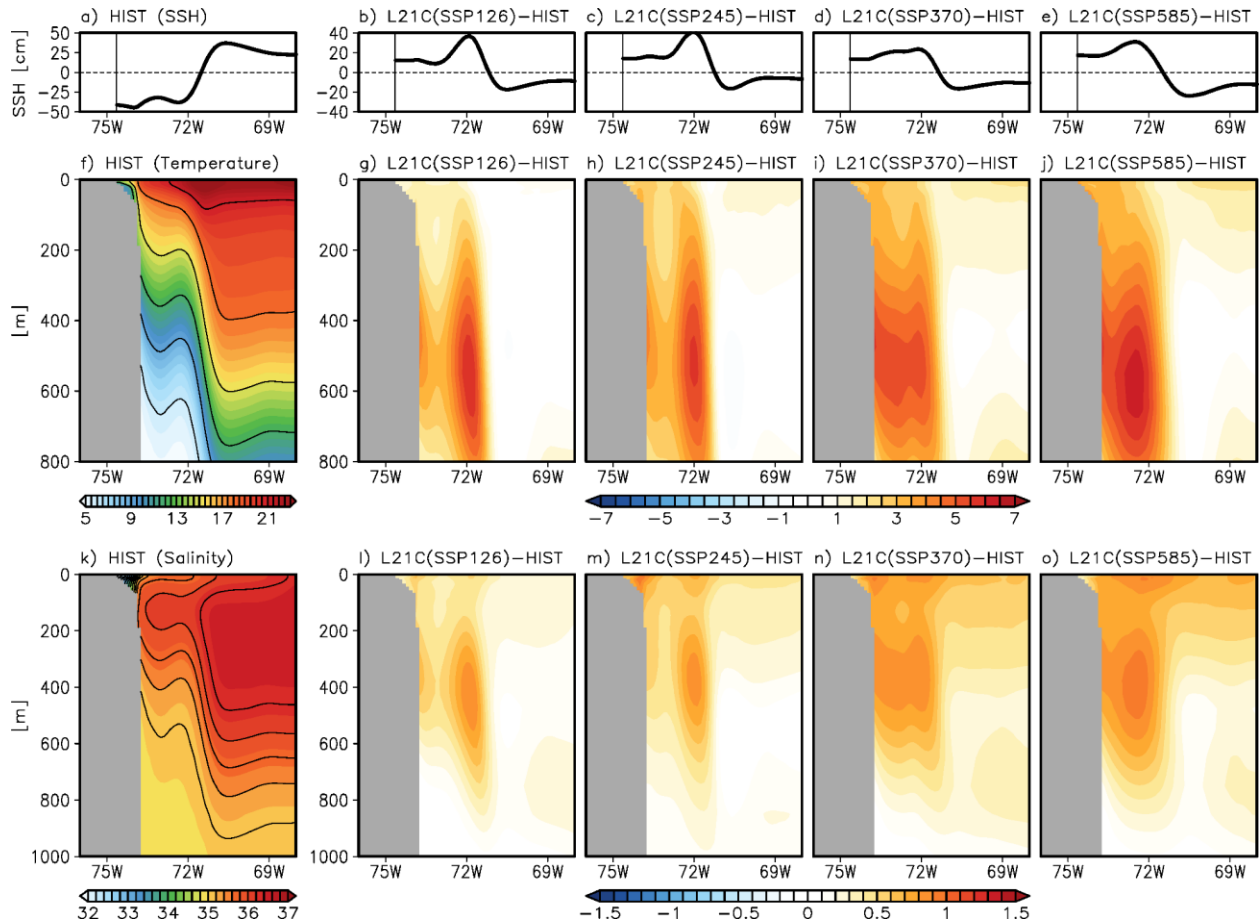
1185  
 1186  
 1187  
 1188  
 1189  
 1190  
 1191  
 1192  
 1193  
 1194  
 1195  
 1196  
 1197  
 1198  
 1199  
 1200  
 1201  
 1202  
 1203  
 1204

**Fig. 15.** (a) Sea level at the east coast of Florida (26.5°N, 79.7°W-78.0°W) during the historical period. Future change in the sea level at the east coast of Florida from (b) SSP-126, (c) SSP-245, (d) SSP-370, (e) SSP-585, and (c) SSP-585 simulations. (f) The vertical cross-sections of the mean temperature across the east coast of Florida during the historical period. The difference in temperature between the future and historical periods from (g) SSP-126, (h) SSP-245, (i) SSP-370, and (j) SSP-585 simulations, respectively. (k)-(o) are the same as (f)-(j) but for salinity.



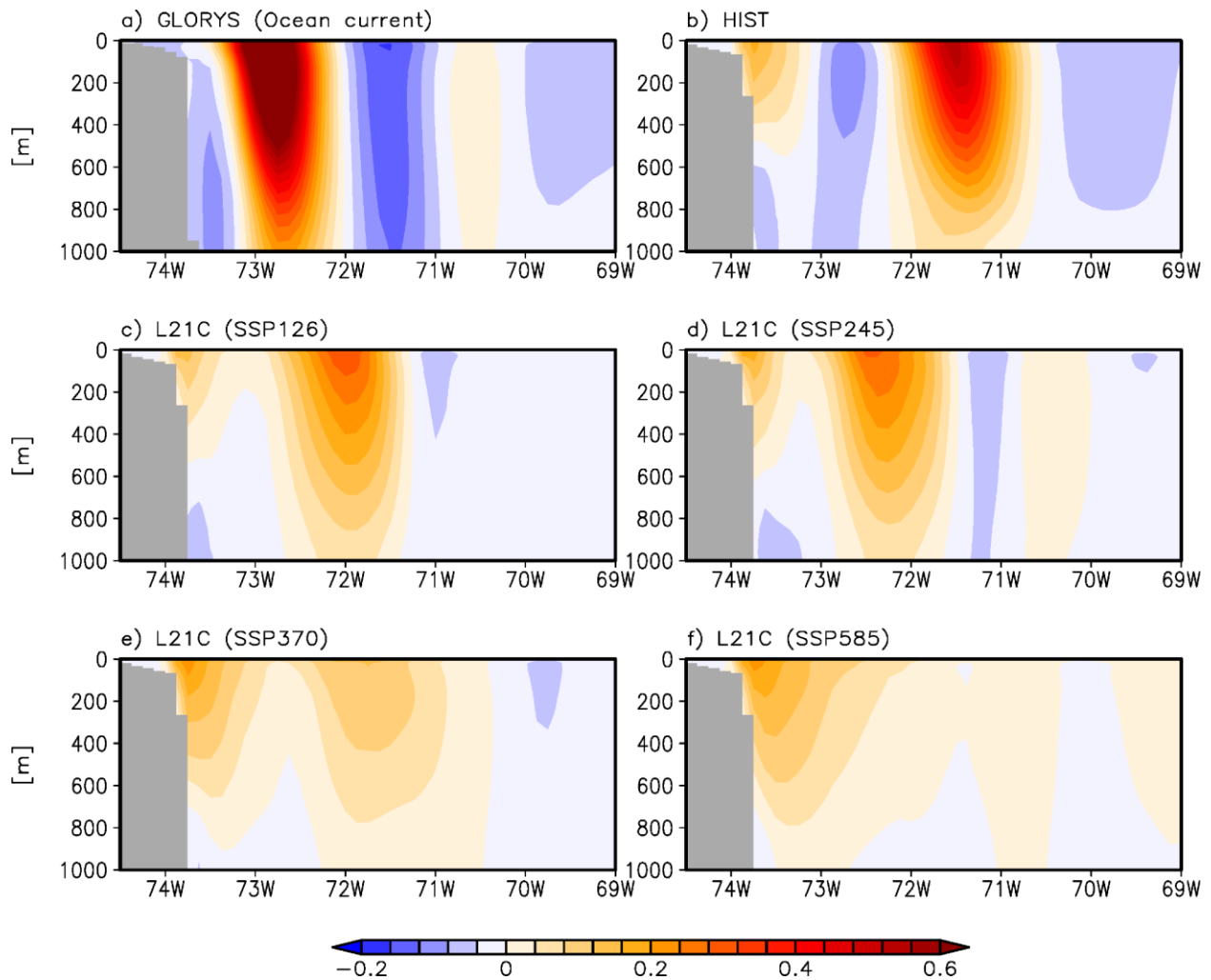
1205  
 1206  
 1207  
 1208  
 1209  
 1210  
 1211  
 1212  
 1213  
 1214  
 1215  
 1216  
 1217  
 1218  
 1219  
 1220  
 1221  
 1222  
 1223  
 1224

**Fig. 16.** (a) Sea level at West Florida ( $26.5^{\circ}\text{N}$ ,  $88^{\circ}\text{W}$ - $81^{\circ}\text{W}$ ) during the historical period. Future change in the sea level at West Florida from (b) SSP-126, (c) SSP-245, (d) SSP-370, (e) SSP-585, and (c) SSP-585 simulations. (f) The vertical cross-sections of the mean temperature ( $^{\circ}\text{C}$ ) across West Florida during the historical period. The difference in temperature between the future and historical periods from (g) SSP-126, (h) SSP-245, (i) SSP-370, and (j) SSP-585 simulations, respectively. (k)-(o) are the same as (f)-(j) but for salinity (psu).



1225  
 1226  
 1227  
 1228  
 1229  
 1230  
 1231  
 1232

**Fig. 17.** (a) Sea level at the MAB ( $30^{\circ}\text{N}$ - $41^{\circ}\text{N}$ ,  $76^{\circ}\text{W}$ - $67^{\circ}\text{W}$ ) during the historical period. Future change in the sea level at the MAB from (b) SSP-126, (c) SSP-245, (d) SSP-370, (e) SSP-585, and (c) SSP-585 simulations. (f) The vertical cross-sections of the mean temperature ( $^{\circ}\text{C}$ ) across the MAB during the historical period. The difference in temperature between the future and historical periods from (g) SSP-126, (h) SSP-245, (i) SSP-370, and (j) SSP-585 simulations, respectively. (k)-(o) are the same as (f)-(j) but for salinity (psu).



1233

1234 **Fig. 18.** (a) Vertical cross-section of the mean alongshore current across the MAB (30°N-41°N,  
 1235 76°W-67°W) during the historical period (1993-2020) from GLORYS12. (b) Same as (a), but for  
 1236 MOM6-NWA12. (c)-(f) are the same as (b), but for the future period (2073-2100) from the (c)  
 1237 SSP1-2.6, (d) SSP2-4.5, (e) SSP3-7.0, and (f) SSP5-8.5 simulations, respectively.